

RESEARCH ARTICLE



Targeting the integrin beta 1-focal adhesion kinase axis with artemisinin: Biophysical disruption of cell adhesion, migration, and invasion in tongue cancer

Laurensia Danis Anggradita ^{1,2} 📵 Joo Hyun Kim ^{2,3} 📵 Min-Kyu Kim ² 📵
Ji Won Son ² Mohd Farhan ² Jothilin Subitsha Alex Jeberson ^{1,2}
Ali Taghizadeh ⁴ Hae-Won Kim ⁴ Jae Hong Park ³ Jaemoon Yang ⁵
Hyung Kwon Byeon ⁶ Sung Sik Hur ² Myung Jin Ban ³ Yongsung Hwang ^{1,2}

Correspondence

Sung Sik Hur, Soonchunhyang Institute of Medi-Bio Science (SIMS), Soonchunhyang University, Cheonan-si 31151, Chungnam-do, Republic of Korea. Email: sstahur@gmail.com

Myung Jin Ban, Department of Otorhinolaryngology—Head and Neck Surgery, College of Medicine, Soonchunhyang University, Cheonan-si 31151, Chungnam-do, Republic of Korea. Email: mjbanent@gmail.com

Yongsung Hwang, Department of Integrated Biomedical Science, Soonchunhyang University, Cheonan-si 31151, Chungnam-do, Republic of Korea. Email: yshwang0428@sch.ac.kr

Abstract

Tongue cancer is a significant threat to human health due to its propensity to spread throughout the oral cavity and to other regions of the head and neck. The challenges posed by its high invasion, metastasis, and late clinical detection underscore the urgency for effective clinical interventions. In this study, we elucidate the promising anti-cancer properties of artemisinin, an anti-malarial drug, in inhibiting cellular interactions within a tongue cancer cell line. Our findings reveal that artemisinin treatment effectively suppresses phosphorylated focal adhesion kinase and its downstream AKT pathway, thereby enhancing apoptotic processes and inducing cell cycle arrest, consequently impeding cellular proliferation. Moreover, artemisinin treatment induces focal adhesion rearrangement and diminishes the cell's capacity to generate traction stress, consequently restraining cell migration on the matrix, as determined via traction force microscopy. Additionally, a transition from N-cadherin to E-cadherin

Laurensia Danis Anggradita, Joo Hyun Kim, and Min-Kyu Kim contributed equally to this study.

VIEW. 2025;20240089. wileyonlinelibrary.com/journal/view 1 of 20

¹Department of Integrated Biomedical Science, Soonchunhyang University, Cheonan-si, Chungnam-do, Republic of Korea

²Soonchunhyang Institute of Medi-Bio Science (SIMS), Soonchunhyang University, Cheonan-si, Chungnam-do, Republic of Korea

³Department of Otorhinolaryngology—Head and Neck Surgery, College of Medicine, Soonchunhyang University, Cheonan-si, Chungnam-do, Republic of Korea

 $^{^4}$ Institute of Tissue Regeneration Engineering (ITREN), Dankook University, Cheonan-si, Chungnam-do, Republic of Korea

⁵Department of Radiology, Yonsei University College of Medicine, Seoul, Republic of Korea

⁶Department of Otorhinolaryngology—Head and Neck Surgery, College of Medicine, Soonchunhyang University, Seoul, Republic of Korea

This is an open access article under the terms of the Creative Commons Attribution License, which permits use, distribution and reproduction in any medium, provided the original work is properly cited.

^{© 2025} The Author(s). VIEW published by Shanghai Fuji Technology Consulting Co., Ltd, authorized by China Professional Community of Experimental Medicine, National Association Health Industry Enterprise Management (CPCEM) and John Wiley & Sons Australia, Ltd.

Funding information

Soonchunhyang University Research Fund; the National Research Foundation of Korea funded by the Ministry of Science and ICT (MSIT), Grant/Award Numbers: 2019R1A5A8083404, RS-2022-NR075792, RS-2023-00284258, RS-2024-00440151, RS-2024-00348582, 2021R1A5A2022318, 2019R1I1A3A01063629 expression occurs at cellular junctions, lowering intracellular stress, as measured by monolayer stress microscopy. This transition significantly curtails cellular migratory capabilities. Our in vivo studies corroborate these findings, showing a significant reduction in tumor volume following artemisinin treatment. Our study highlights the therapeutic potential of artemisinin use as a novel strategy for tongue cancer treatment, which acts via modulating both intracellular and intercellular interactions.

KEYWORDS

artemisinin, migration, monolayer stress microscopy, tongue cancer, traction force microscopy

1 | INTRODUCTION

Oral squamous cell carcinoma (OSCC), a subset of head and neck squamous cell carcinoma (HNSCC), represents the most prevalent form of oral cancer, comprising 90% of all oral malignancies, with a higher incidence reported in males than in females. Although OSCC can manifest in various regions of the oral mucosa, the tongue stands out as the most frequently affected site.² The delayed diagnosis of this disease primarily contributes to the elevated incidence of tongue cancer, often leading to malignancy and increased risk of metastasis to distant anatomical sites.3 The progression to malignancy in tongue cancer is closely linked to the epithelial-to-mesenchymal transition (EMT) process, during which normal cells lose their adherence to the extracellular matrix (ECM), resulting in a transformation marked by heightened motility and invasiveness.4 EMT plays a pivotal role in the local recurrence and metastatic dissemination of tongue cancer and worsens patient prognosis.⁵ For studies on oral squamous cancer, Cal27 is one of the most frequently used cell lines. Cal27 has an epithelial-like phenotype and is a low metastatic cell line, as it expresses EMT markers to a lesser degree compared to other oral cancer cell lines such as SCC9 and SCC25.6

Alteration of intracellular signaling pathways represents one of the several facets contributing to the aggressiveness of tongue cancer. The fibrotic microenvironment of tongue cancer is a significant factor promoting cancer migration, as the rigid matrix induces the expression of transcription factors involved in EMT, promoting accelerated migration. Consistently, extended culture of tongue cancer cells within a stiff niche can heighten migration, indicating the cellular capability to develop mechanical memory, which is crucial for infiltrating surrounding softer tissues from rigid tumors. Mechanotransduction, the process by which cells sense external stiffness and translate it into intracellular responses, involves the acti-

vation of transmembrane proteins such as integrins and focal adhesions (FA), which transmit mechanical signals from the ECM through the cytoskeleton to the nucleus. This mechanistic process dictates various cellular behaviors, including cell spreading, proliferation, lineage commitment, and the EMT process crucial for cancer migration. Numerous studies have highlighted the role of stiffness-sensing in modulating FA and activation of the PI3K/AKT signaling pathway during the EMT.

Innovative tools for investigating mechanobiology were pioneered by Harris et al., ¹⁴ who introduced traction force microscopy (TFM) as a means to quantify forces and stress between cells and their underlying ECM. ¹⁵ Cells exert forces on the ECM to regulate cellular characteristics such as morphology and migration. ¹⁶ Further advancements by Tambe et al. ¹⁷ and Hur et al. ¹⁸ facilitated the mapping of not only cell–matrix forces but also intracellular forces using monolayer stress microscopy (MSM). This technique enables the quantification of stress exerted within and between cells in a monolayer configuration. ¹⁹ Current understanding suggests that in a monolayer, individual cells exert local physical forces, which collectively contribute to a global tensile stress that propels the movement of the entire cell sheet. ²⁰

Artemisinin, derived from the Chinese plant *Artemisia annua*, ²¹ is renowned for its multifaceted effects in inhibiting cellular inflammation, ²² proliferation, ²³ and migration. ²⁴ Recently, considerable attention has been directed toward exploring its therapeutic potential as an anticancer agent. ²⁵ Artemisinin can impede the proliferative capacity and EMT processes by upregulating E-cadherin expression and downregulating vimentin in ovarian cancer. ²⁶ Additionally, the inhibition of the PI3K/AKT/mTOR signaling pathway by artemisinin can suppress the migratory and invasive capabilities of uveal melanoma cells, consequently restraining tumor growth in vivo. ²⁷ Similarly, artemisinin and its derivatives, such as dihydroartemisinin, inhibit the proliferation and

migration of OSCC cells through the regulation of reactive oxygen species production.²⁸ Despite these advances, the role of these compounds in modulating the mechanotransduction pathway in OSCC remains largely unexplored. Therefore, to address this gap in the present study, we aimed to elucidate the potential role and anti-tumor effects of artemisinin in tongue cancer using the Cal27 cell line and provide a proof-of-concept to establish its candidacy as an anticancer agent to mitigate cancer cell growth, migration, and invasion.

In this study, we employed TFM and MSM, using polyacrylamide (PAA) with varying stiffnesses to recapitulate the tumor microenvironment (TME) and to measure cellular forces. This approach facilitated the investigation of mechanotransduction processes, encompassing the inhibition of integrin and FA complex to modulate cell behavior. Collectively, our findings highlight the pivotal role of artemisinin in modulating both intercellular and intracellular interactions to impede EMT and further establish its potential as a novel therapeutic agent for oral cancer.

2 | RESULTS AND DISCUSSION

2.1 | Artemisinin significantly reduces proliferation, viability, and motility of Cal27 cells in vitro

Given that cancer is characterized by uncontrolled cell division, assessing efficacy of potential therapeutic agents often involves evaluating their ability to inhibit cell proliferation and induce cytotoxicity in cancer cells.²⁹ Artemisinin and its derivatives have shown anticancer effects in ovarian cancer cells³⁰ and lung carcinoma,³¹ although their impact on oral cancer remains unvalidated. In this study, we conducted various assays to investigate the effects of artemisinin on Cal27 cells. Initially, we determined the effect of 50 µM artemisinin treatment on the viability and proliferation of Cal27. Compared to the control group, cell viability of the treatment group decreased by only 2% (Figure 1A,B), indicating that treatment with 50 µM artemisinin did not significantly affect cell viability. However, proliferation assays conducted every 24 h over a span of 3 days revealed that cellular proliferation decreased by 14.35% at 48 h and 26.78% at 72 h in the artemisinintreated group (Figure 1C,D). These results demonstrate that 50 µM artemisinin mildly reduces cell proliferation after a 24-h treatment.

Artemisinin can arrest the cell cycle in tumor cells, primarily by disrupting cell cycle kinetics or impeding pathways involved in cellular proliferation.³² In our study, artemisinin treatment led to a substantial (>40%) arrest of cells in the S phase during DNA replication, as demon-

strated using FACS analysis (Figure 1E,F). Consistent with findings published earlier, ^{23,33} artemisinin also induced G1 phase cell cycle arrest, preventing cells from progressing into the S phase, thereby attenuating the proliferation of tongue cancer cells. Artemisinin can enhance apoptosis by activating phosphorylated-p38 mitogen-activated protein kinase in lung carcinoma. ³⁴ In our study, we also observed anti-proliferative activity of artemisinin (Figure 1G,H). Additionally, a colony formation assay followed by crystal violet staining over a 2-week period revealed the formation of 86 colonies in the control group, whereas only 11 colonies (87.21% reduction) of smaller size formed in the artemisinin-treated group. These findings underscored the significant inhibitory effect of artemisinin on colony formation by cancer cells.

2.2 | Artemisinin inhibits cell migration and invasion

Cell migration facilitates cancer invasion into surrounding tissues during metastasis.³⁵ Initially, we performed Transwell assays to assess cell migration and invasion, with the total area quantified through crystal violet staining (Figure 2A,C). Compared to the control group, artemisinin treatment led to a 54.05% reduction in the area covered by migrating cells (Figure 2B) and a 47.13% reduction in cell invasion (Figure 2D). Subsequently, a wound-healing assay was conducted at 12-h intervals over 24 h. As depicted in Figure 2E, both the control and artemisinin-treated groups exhibited similar wound gaps at 0 h. However, after 24 h, the control group demonstrated $98.61\% \pm 1.39\%$ wound healing, whereas the artemisinin-treated group exhibited only $71.18\% \pm 7.28\%$ wound healing (Figure 2F). Notably, these results suggest that although treatment with 50 µm artemisinin did not affect the viability of Cal27, it effectively mitigated their motility. Artemisinin effectively inhibits cell migration in uveal melanoma,²⁷ breast cancer, 36 and hepatocellular carcinoma. 37 Given the pivotal role of migration in cancer cell metastasis and inflammation, the suppression of Cal27 migration following artemisinin treatment holds significant therapeutic implications. Moreover, these results implicate the potential of artemisinin-based therapies for the prevention and treatment of metastasis in head and neck cancer (HNSC).

2.3 | Artemisinin inhibit FAK/PI3K/AKT pathway

The intricate molecular mechanisms governing cancer cell migration and invasion are finely intertwined with cell-matrix interactions, orchestrated by complex

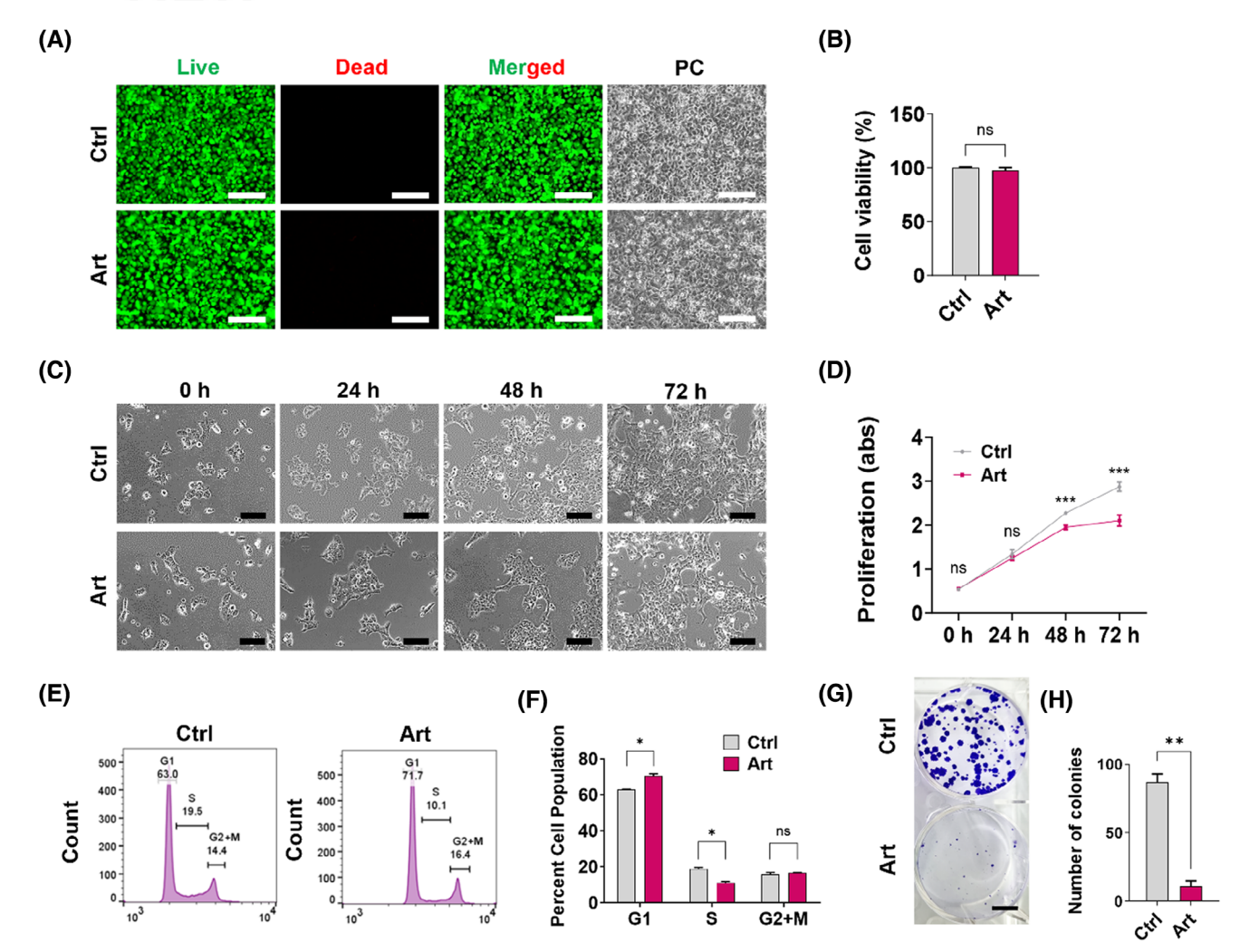


FIGURE 1 Impact of artemisinin on Cal27 cell proliferation and motility. (A) Live/dead cell viability assay of Cal27 cells cultured on tissue culture plates (TCP) and treated with 50 μ M artemisinin for 4 h (Art group). Green and red signals depict live and dead cells, respectively. Scale bar: 150 μ m. (B) Quantification of Cal27 cell viability after 4 h exposure to artemisinin, based on image analysis of the Live/Dead assay. (C and D) Cal27 cell proliferation at 0, 24, 48, and 72 h after treatment using MTT assays. Scale bar: 150 μ m. (E and F) Cell cycle analysis conducted using FxCycle staining after 48 h exposure to artemisinin. (G and H) Colony formation assay using Cal27 cells over 14 days. Scale bar: 5 mm. Data are presented as the mean \pm standard error of the mean (SEM). *p < .05, **p < .01, ***p < .001.

signaling pathways and cellular constituents.³⁸ By analyzing the HNSCC TCGA database, we identified elevated expression of integrin beta 1 (ITG β 1) and FA kinase (FAK) in tumor tissues (FAK: increase of 7%, ITG β 1: increase of 5%), correlating with lower patient survival rates (Figure 3A,B). Subsequent histological and immunohistochemical assessments of biopsies from human HNSC tissue and adjacent normal tissue corroborated the fibrosis and overexpression of α SMA, FAK, ITG β 1, and Collagen-1 proteins in cancerous tissues (Figure 3C, Figure S1), consistent with findings in other cancer types such as esophageal squamous cell carcinoma,³⁹ breast cancer,⁴⁰ and ovarian cancer.⁴¹ ITG β 1 is a pivotal mediator facilitating cellular adhesion to the ECM. Its interaction with ECM components can also trigger intracellular signaling cascades that

govern intricate cellular processes, including migration and invasion.⁴² Upon ECM binding, ITG β 1 activation initiates FA formation, involving the activation of FAK and its downstream pathways.⁴³

Based on these observations, we posited that artemisinin treatment might impede cell migration by regulating the ITG β 1/FAK pathway and its downstream signaling. Artemisinin treatment attenuated ITG β 1 and FAK phosphorylation (Tyr397), revealing its role in modulating ITG β 1/FAK pathway activity (Figure 3D–F). Inhibition of FAK has been associated with decreased migration and metastasis in breast cancer cells.⁴⁴ Consistently, we also noted the downregulation of the downstream ITG β 1/FAK pathways, specifically phospho-PI3K (Tyr607) and phospho-AKT (Ser473) pathways,

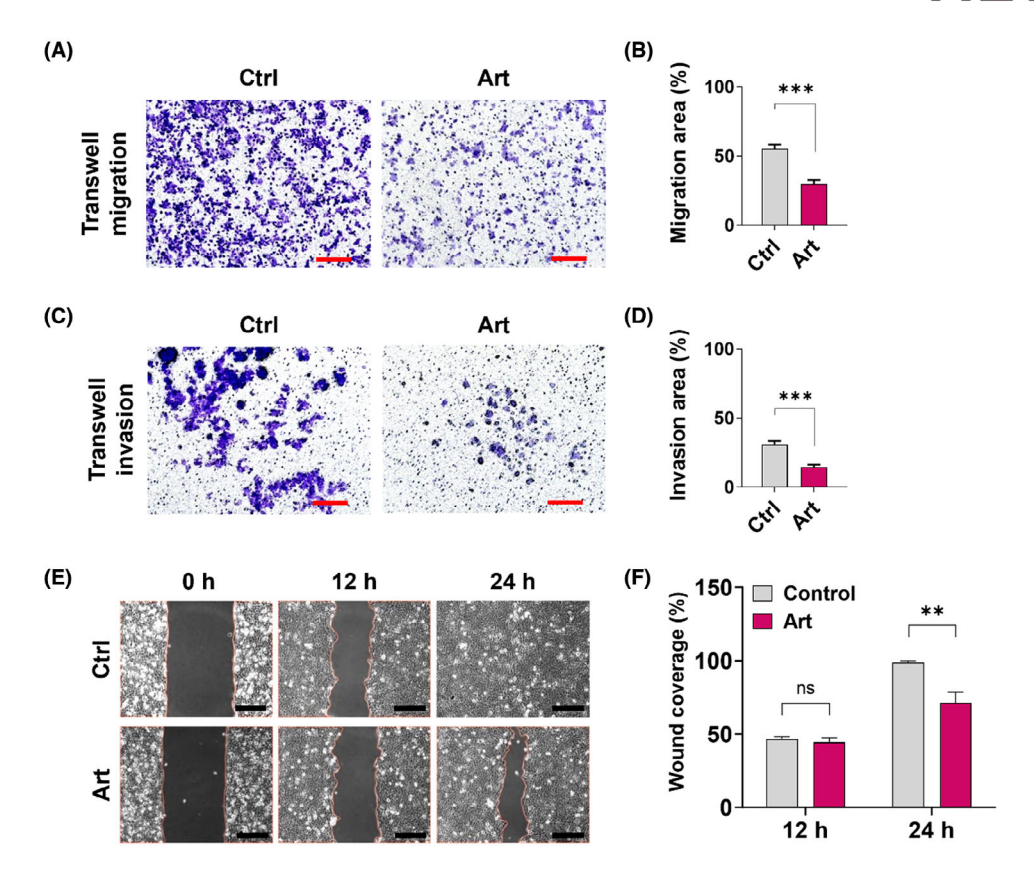


FIGURE 2 Suppression of cell migration and invasion following artemisinin treatment. (A and B) Reduced migration of cells through the Transwell membrane 12 h after artemisinin treatment. Scale bar: 200 μ m. (C and D) Decreased invasion of cells through Matrigel following 24 h of artemisinin treatment. Scale bar: 200 μ m. (E and F) Inhibition of cell migration observed 12 and 24 h post-artemisinin treatment. Scale bar: 150 μ m. Data are presented as mean \pm standard error of the mean (SEM). * *p < .05, * *p < .01, * *p < .001.

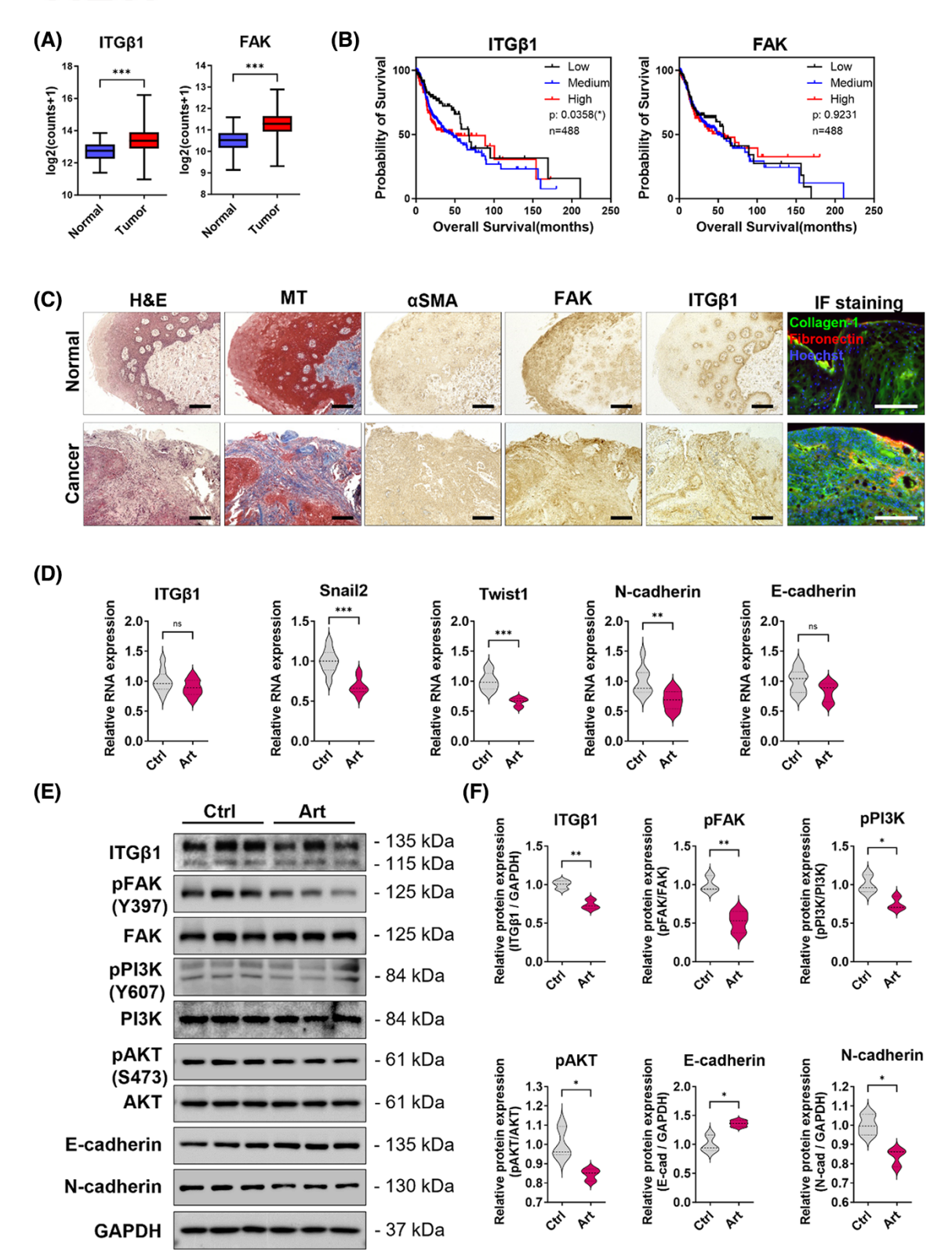
following artemisinin treatment, mirroring findings in uveal melanoma.²⁷ AKT phosphorylation is implicated in cell survival, proliferation, adhesion, and migration.⁴⁵ We also observed a decreased expression of EMT-related transcription factors such as Snail2 and Twist1 following artemisinin treatment (Figure 3D). Artemisinin is known to counteract the EMT by targeting E-cadherin and vimentin in ovarian cancer.²⁶ Furthermore, artemisinin modulated the expression of intercellular junctions by downregulating neural cadherin (N-cadherin) and upregulating epithelial cadherin (E-cadherin) expressions. The transition between N- and E-cadherin is a hallmark of the EMT process where the interactions are also regulated by the PI3K pathway during migration.⁴⁶

2.4 | Artemisinin inhibits FAK expression, cell-matrix adhesion, and migration

To better define the distinctive characteristics of the ECM in normal and cancerous environments, we next investigated cell-ECM interactions. To simulate collagen

deposition in the TME, we cultured cells on PAA gels with two stiffness levels: 2.55 kPa, resembling the softness of healthy tongue tissue, 47 and 49.4 kPa, representing the stiffness typical of a cancerous environment attributed to elevated ECM production (Figure 4A,B).^{47,48} Initially, the higher matrix stiffness induced the migration of Cal27 cells, as revealed by greater cellular movement on rigid matrices (0.85 \pm 0.10) compared to movement on soft matrices (0.61 \pm 0.06) (Figure 4C; Videos S1-S4 and Figure S2A), which was consistent with previous studies highlighting the heightened migratory capacity of HNSC cells in response to substrate stiffening.⁴⁹ Furthermore, artemisinin treatment-induced differential single-cell migration in different matrixes, approximately 33% in soft matrix and 23% rigid matrix, indicating a slower cell migration rate on both matrices. These findings suggest that artemisinin treatment inhibits movement of single Cal27 cells across matrixes of varying stiffnesses. In addition, the movement was slower in the rigid matrix where the migration is restricted due to the rigid condition.

We further observed evidence of actin remodeling as shown by increased F-actin (47%) and phosphorylated



FAK (p-FAK) (12.7%) intensity along the cellular edges during cell spreading across the rigid matrix (Figure 4D–H, Figure S2B). These findings align with those of previous research studies indicating that a stiff matrix promotes stable actin structures, facilitating cell elongation.⁵⁰ FAK-

mediated integrin activation regulates cell migration, as integrin assembly occurs during the protrusion of migrating cells, and its turnover is crucial for cellular retraction during migration.⁵¹ The regulation of cell spreading in response to different matrix stiffness demonstrates the

mechanosensing behavior of Cal27 cells, whereby they react to a stiff matrix by altering their behavior, including increased spreading,⁵² proliferation,⁵³ and migration.⁵⁴ Alterations in cellular morphology was evidenced by increased surface area (481.2 \pm 20.77 μ m²) and the lengthening of the major axis $(27.75 \pm 0.67 \,\mu\text{m})$ on rigid matrices compared to those on soft matrices (344.2 \pm 16.41 μ m and $24.05 \pm 0.70 \, \mu m^2$) (Figure 4I–K). Additionally, we noted a decrease in cell circularity on rigid matrices (0.55 ± 0.1) compared with that on soft matrices (0.64 \pm 0.11) (Figure S2C). Cells cultured on rigid gels generally exhibit greater spreading, resulting in increased cellular area for adhesion and interaction with the underlying matrix.⁵⁵ Consistently, we also observed higher stress (21%) and intracellular tension (22.5%) in the rigid matrix (Figure 4L-N), indicating that the cells had the ability to adapt their internal mechanics to varying matrix stiffnesses. Moreover, cellular viscoelastic changes observed as higher cellular stiffness (6%) in the rigid matrix (Figure 4N) aligned with the higher cellular and stress.

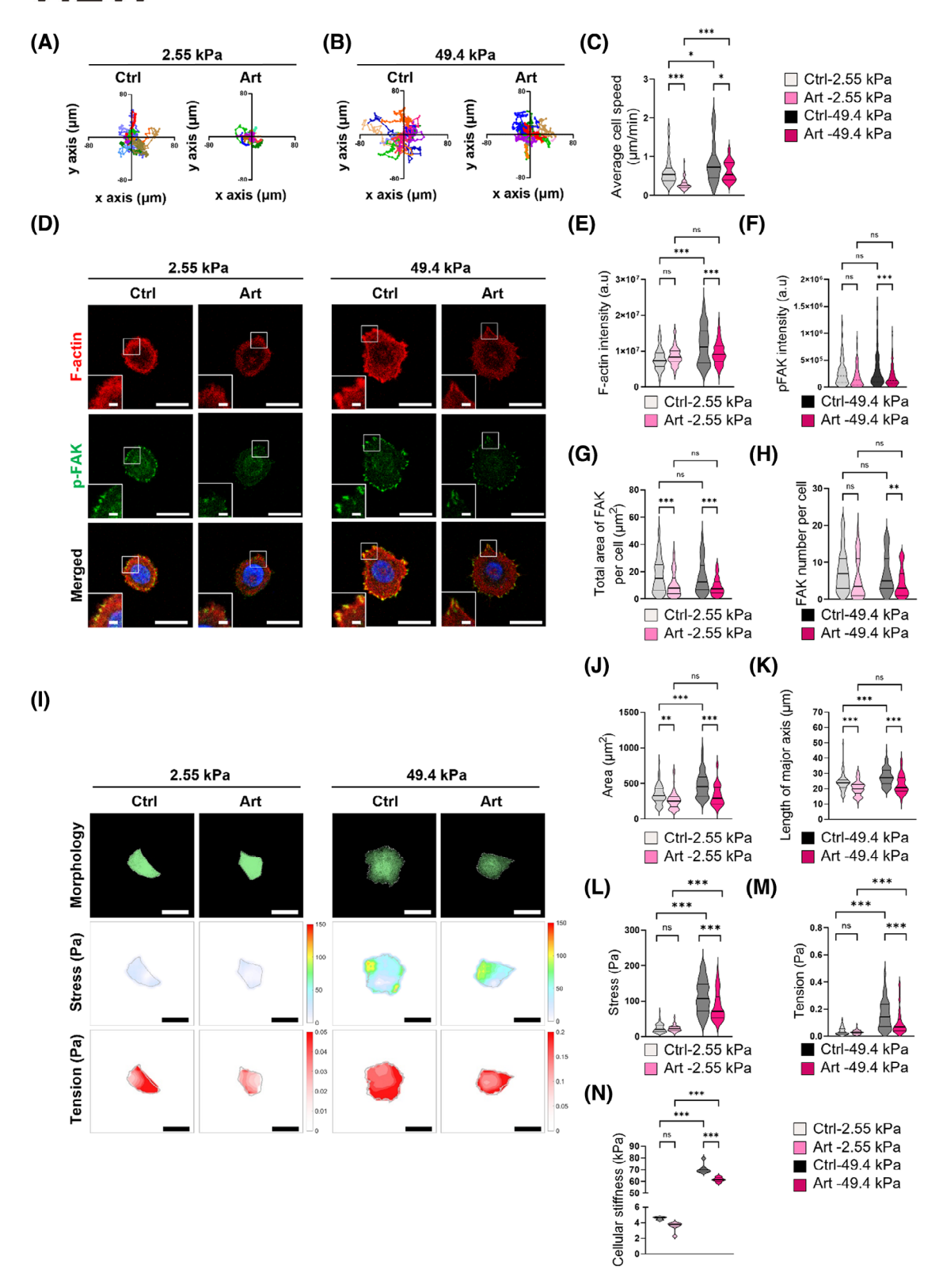
Intracellular tension plays a pivotal role in cell adhesion by governing the positioning of adhesions at the leading edge of lamellipodia during cell migration.⁵⁶ In our study, artemisinin treatment reduced cell-matrix adhesion. Artemisinin suppressed FAK phosphorylation, as evidenced by decreased p-FAK intensity (soft matrix: 30%, rigid matrix: 36%) and reduced stress fibers size (soft matrix: 6.67 µm², rigid matrix: 7.42 µm²) compared to those in the control group. Additionally, artemisinin attenuated the formation of FAs, consequently diminishing cellmatrix adhesion. Furthermore, artemisinin treatment also decreased the cell area (soft matrix: 24%, rigid matrix: 32%) and the major axis of the cell (soft matrix: 16%, rigid matrix: 18%), resulting in diminished cellular spreading and lesser area available for cell attachment and adhesion to the matrix. Consequently, a decrease in cellular stress (24.7%), tension (35.2%), and stiffness (13%) was observed following artemisinin treatment in the rigid matrix. Although the decrease by artemisinin treatment was less pronounced in the soft matrix, a decrease was still evident posttreatment, reaffirming the role of artemisinin in diminishing cell-matrix interactions in tongue cancer cells, thereby reducing cellular spreading and minimizing the area available for adherence to the matrix. Aligned with the stress response, the softening of the cells also suppresses cellular spreading onto the matrix.⁵⁷

2.5 | Artemisinin and soft substrates inhibit traction and intracellular stresses leading to reduced cell migration

We investigated collective cell movement using a woundhealing assay on substrates of varying stiffnesses (2.55 kPa for soft and 49.4 kPa for stiff). Our findings revealed that increased substrate stiffness led to a respective 28% and 25% enhancement in migration at 12 and 24 h (Figure 5A,B). Additionally, artemisinin treatment notably inhibited cell migration, with 47% and 46% lower migration on soft substrates, and 36% and 26% lower migration on stiff substrates, at 12 and 24 h, respectively. This highlights the significant effect of artemisinin, particularly during the initial stages of collective migration. Our results suggest that collective cell migration can be impeded by both reducing substrate stiffness and artemisinin treatment. These findings align with our observations regarding single-cell movement (Figure 4K-M). Furthermore, we observed a deceleration in collective migration as the size of the wound gap diminished. Notably, artemisinin exerted inhibitory effects on cell migration on both soft and stiff substrates, highlighting its role not only in modulating single cell-matrix interactions but also in affecting cellcell interactions during collective cell migration. These results underscore the potential of artemisinin as an anticancer agent, consistent with previous findings in uveal melanoma.⁵⁸

Next, to evaluate the impact of mechanical forces on wound healing, we conducted cellular force analyses on collectively migrating cells across a 500-µm wound gap. We assessed cell–ECM stress (traction stress) on both soft and

FIGURE 3 Effects of artemisinin treatment on the focal adhesion kinase (FAK)/PI3K/AKT pathway and epithelial-to-mesenchymal transition (EMT) markers in Cal27 cells. (A) FAK and integrin beta 1 (ITG β 1) transcript levels in normal and tumor tissues from HNSC TCGA dataset. Sample sizes: normal = 44, tumor = 520. (B) Kaplan-Meier analysis evaluating the overall survival of HNSC patients. Samples were stratified into three groups based on FAK and ITG β 1 expression levels, with divisions set at the top 25%, bottom 25%, and middle 50% according to a quartile test. (C) Comparison of fibrosis in tongue cancer tissue versus normal tissue as shown by hematoxylin and eosin (H&E) staining and immunohistochemistry images of α SMA, FAK, ITG β 1, fibronectin, and collagen-1 expression in normal and HNSC tissues. Scale bar: 200 µm. (D) qRT-PCR analysis of ITG β 1, EMT markers (Snail2, Twist1, N-cadherin), and E-cadherin expression upon treatment with 50 µM artemisinin in Cal27 cells compared to control cells. Sample size: n = 3. (E) Immunoblot analysis were performed using 50 µM artemisinin-treated and control cells showing phospho-FAK (Tyr397), FAK, phospho-PI3K (Tyr607), PI3K, phospho-AKT (Ser473), AKT, ITG β 1, E-, and N-cadherin expression; GAPDH expression was used as a loading control. Artemisinin treatment for qRT-PCR and immunoblot analyses was conducted for 24 h (n = 3). (F) Relative quantification of immunoblot data. Data are presented as the mean \pm standard error of the mean (SEM). *p < .05, **p < .01, and ***p < .001.



rigid matrices at 0 and 12 h post-injury. Notably, substrate stiffness significantly augmented traction stress levels by 1854% and 953% at 0 and 12 h, respectively. However, treatment with artemisinin mitigated these increases by 751% and 430% at 0 and 12 h, respectively (Figure 5C,E). A

schematic depiction of traction stress magnitude is shown in Figure 5D. Artemisinin decreased traction stress by 26% on soft substrates and 68% on stiff substrates at 0 h, with a lesser impact observed at 12 h. These findings suggest that the impact of artemisinin on traction stresses

diminishes as the wound gap closes, mirroring its effects on wound-healing kinetics.

Our findings collectively demonstrate a tight correlation between cell-matrix forces and collective cell migration in the wound-healing assay. Consistent with another study, which highlighted that matrix rigidity contributes to the invasion of breast cancer cells via the integrin/FAK mechanotransduction pathway,⁵⁹ we observed that lower substrate stiffness and artemisinin treatment were associated with reduced cell-ECM stresses, which led to decreased cell migration. Moreover, artemisinin exhibited greater efficacy at earlier time points.

We also investigated maximum shear stress (IS_{maxshear}, Figure 5G) as a quantitative measure of intracellular stress (IS) anisotropy, as reported previously. 17 Elevated values of maximum shear IS typically correlate with accelerated directional migration toward the wound. Interestingly, intracellular maximum shear stresses were heightened on stiff substrates but diminished upon artemisinin treatment. Additionally, we noted a decrease in the disparity of maximum intracellular shear stress as the wound gap narrowed. This trend is consistent with observations related to collective cell migration (Figure 5B), traction stress (Figure 5C-E), and IS levels (Figure 5F-J). Traction stress plays a pivotal role in regulating cellular displacement during migration.⁶⁰ Consistent with our findings, inhibition of traction stress was reported to reduce alterations in cell shape and collective migration of MCF10A breast cancer epithelial cells.⁶¹ Importantly, decreased traction stress, coupled with reduced FA turnover, inhibits downstream regulatory events, leading to diminished migration. 62

2.6 | Artemisinin attenuates tumor growth in Cal27 xenograft mouse model

To explore the anticancer effects of artemisinin on tongue cancer, we utilized subcutaneous xenograft tumor models established with Cal27 cells. The methodology for tumor generation, measurement, and treatment is described in Figure 6A. Upon reaching a volume of 100 mm³, tumors were treated with artemisinin, cisplatin (as a positive con-

trol), or dimethyl sulfoxide (DMSO) (vehicle control) over a period of 21 days. Posttreatment analysis revealed significant reductions in tumor volume: the DMSO group exhibited an average volume of $366.46 \pm 222.12 \text{ mm}^3$, whereas the artemisinin and cisplatin groups demonstrated volumes of 161.33 ± 84.54 and $103.57 \pm 26.94 \text{ mm}^3$, respectively. This corresponds to a 56% reduction in tumor volume for artemisinin and a 71.75% reduction for cisplatin when compared to the DMSO group (Figure 6B,C). Further assessments posttreatment showed a decrease in tumor weight by 24.36% in the artemisinin group and 47.43% in the cisplatin group compared to the DMSO control (Figure 6D,E). These results indicate that both artemisinin and cisplatin effectively suppress tumor growth in the Cal27 xenograft model.

In addition, to evaluate the potential toxicity of the treatments, changes in body weight were monitored. Mice in the cisplatin group exhibited significant weight loss (26.52% reduction), aligning with known side effects such as gastrointestinal disturbances and nephrotoxicity.⁶³ In contrast, the artemisinin-treated mice showed minimal weight loss (5.31% reduction), suggesting a more favorable safety profile compared to cisplatin (Figure 6F). These findings corroborate previous studies that have documented the anticancer efficacy of artemisinin and its derivatives across diverse cancer models. Notably, studies have demonstrated that these compounds can suppress tumor growth in non-small cell lung cancer by inhibiting cellular proliferation and reducing malignancy.⁶⁴ Our findings extend this therapeutic potential to HNSCC, suggesting that artemisinin could serve as an effective alternative or adjunct to traditional chemotherapy regimens. Importantly, unlike cisplatin, which is associated with significant toxicity and adverse effects, artemisinin was characterized by only minimal weight loss in treated mice (5.31% reduction), indicating a superior safety profile. This observation corroborates reports highlighting artemisinin's relative safety and lower incidence of side effects compared to conventional chemotherapy agents.⁶⁵ Thus, our study supports the further exploration of artemisinin as a promising candidate for less toxic cancer treatment strategies.

FIGURE 4 Artemisinin modulates integrin-mediated focal adhesion kinase (FAK) activity to diminish cell-matrix stress and migration. (A–C) Validation of reduced epithelial-to-mesenchymal transition (EMT) through diminished single-cell migration 12 h of after artemisinin treatment. (D–H) Immunofluorescent images illustrating focal adhesion and cytoskeleton remodeling post-artemisinin treatment, as evidenced by intensity and quantification of FAK area. Scale bar: $25 \mu m$. n = Ctrl soft: 152, Art soft: 97, Ctrl stiff: 138, Art stiff: 126. (I) Artemisinin influences cellular stress and tension, leading to alterations in cellular morphology. Scale bar = $25 \mu m$. (J and K) Reduction in cellular area and length of the major axis following artemisinin treatment. (L and M) Artemisinin-mediated regulation of cellular stress and tension across matrices of varying stiffnesses. n = Ctrl soft: 65, Art soft: 68, Ctrl stiff: 75, Art stiff: 46. (N) Softening of Cal27 cells post-artemisinin treatment as assessed by nanoindenter. n = Ctrl soft: 6, Art soft: 7, Ctrl stiff: 7, Art stiff: 8. Immunofluorescence, cell shape analysis, stress, and tension measurements were conducted on cells treated with artemisinin for 24 h (Art) or untreated controls (Ctrl). Data are presented as mean \pm standard error of the mean (SEM). *p < .05, **p < .01, and ***p < .001.

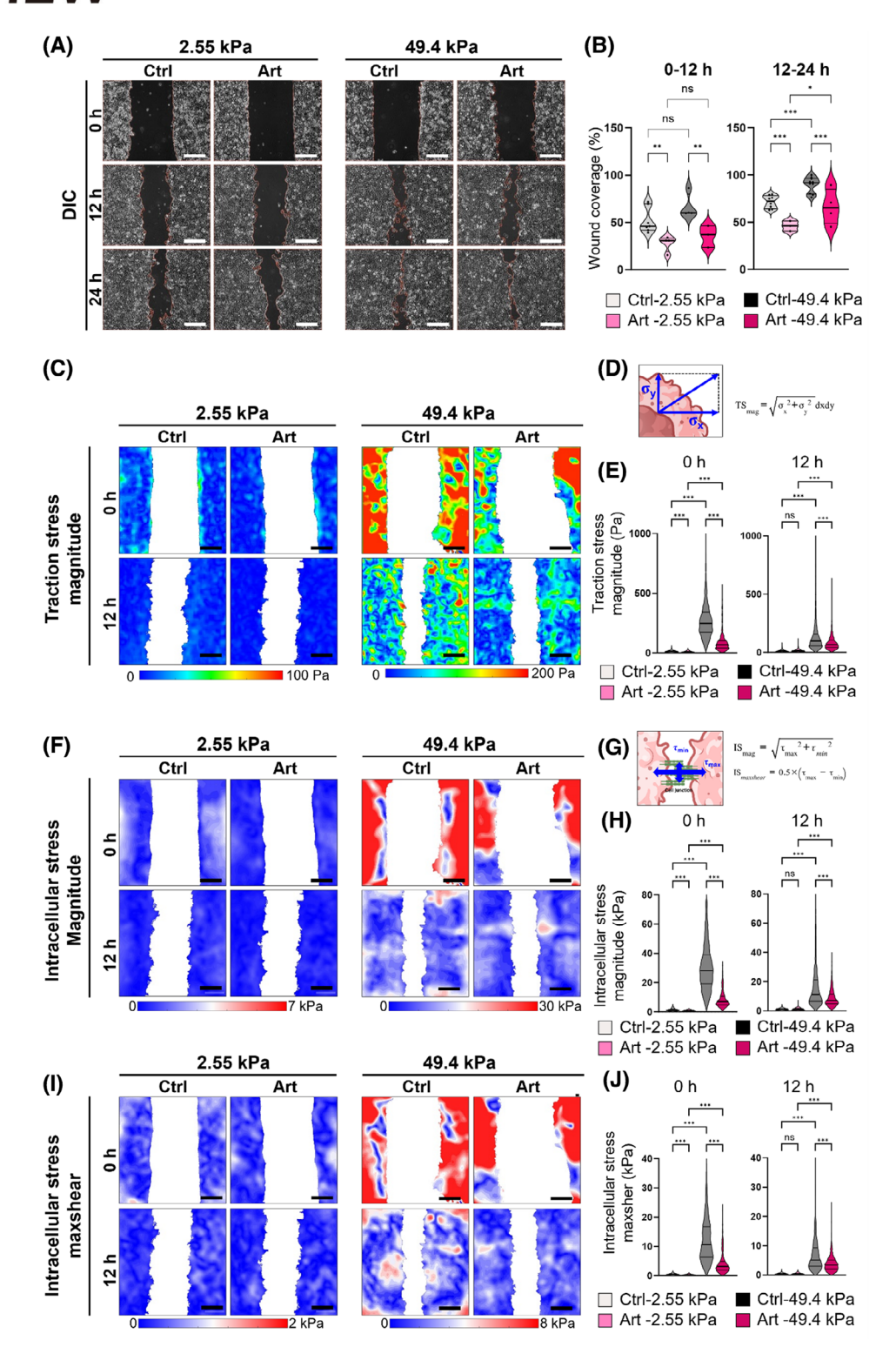


FIGURE 5 Artemisinin inhibits collective cell migration by regulating cell–matrix and cell–cell stress within cell monolayer. (A and B) Reduction in collective cell migration of Cal27 cancer cells following artemisinin treatment for 24 h. Scale bar: 150 μ m. n = Ctrl soft: 7, Art soft: 4, Ctrl stiff: 4, Art stiff: 3 (0–12 h), Ctrl soft: 8, Art soft: 3, Ctrl stiff: 10, Art stiff: 4. (C and E) Total traction stress (TS_{mag}) indicates decreased cell–matrix stress post-artemisinin treatment at 0 and 12 h. (D) Schematic depiction of traction stress within collective cells. (F and H) Intracellular stress (IS_{mag}) generation at cell junctions controls migration. (G) Schematic representation of calculated intracellular stress. (I and J) Quantification of intracellular maxshear (IS_{maxshear}) to determine isotropy degree. Scale bar: 250 μ m. n = Ctrl soft: 1375, Art soft: 1166, Ctrl stiff: 1271, Art stiff: 905 (0–12 h), Ctrl soft: 987, Art soft: 828, Ctrl stiff: 973, Art stiff: 1135. N numbers represent pixel values from one (0 h) and three biological replicates (12 h). Data depicted in violin plots with lines representing the mean and quartiles. *p < .05, **p < .01, ***p < .001.

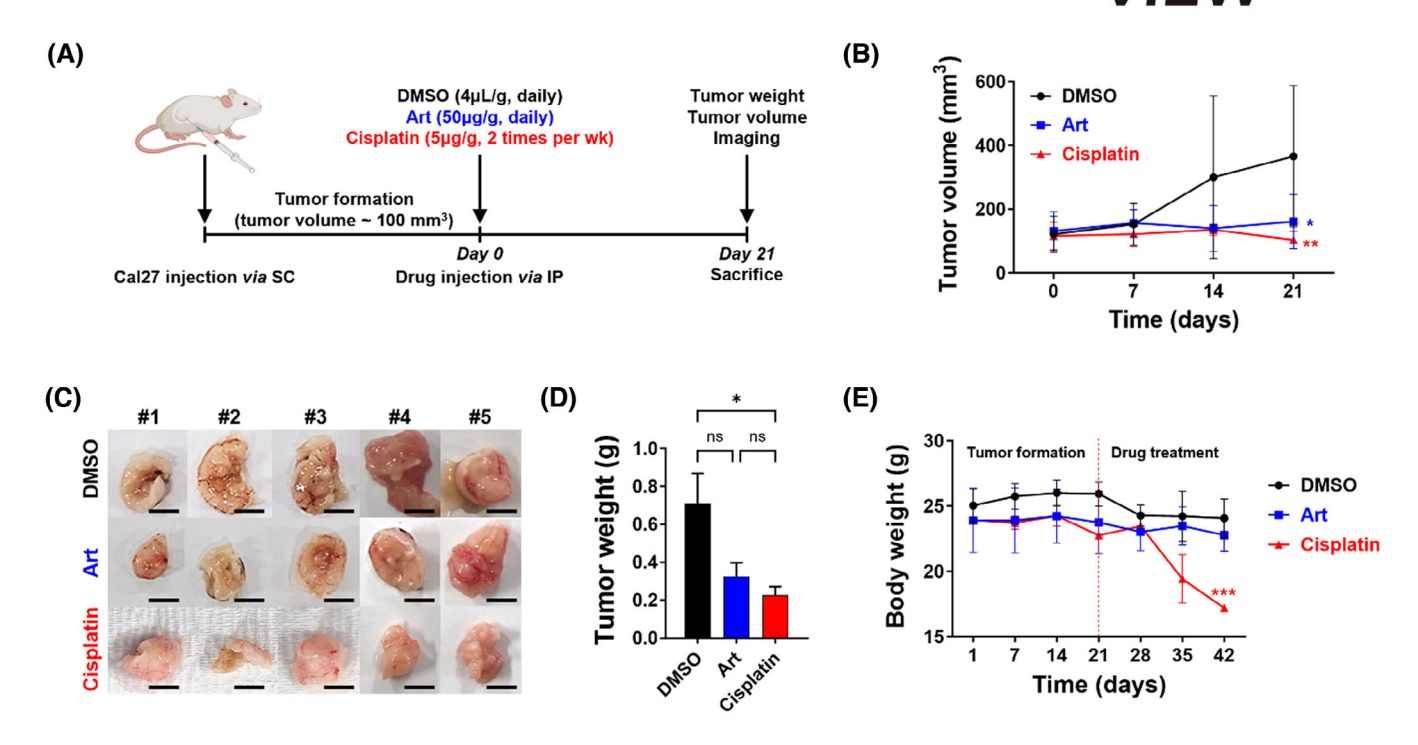


FIGURE 6 Comparative analysis of anticancer effects of artemisinin and cisplatin in a Cal27 xenograft mouse model. (A) Schematic illustration of the experimental setup for evaluating the effects of artemisinin. (B) Changes in tumor volume over the course of treatment in tumor-bearing mice. Tumor volumes were measured posttreatment across different groups. (C) Representative images of tumors from the dimethyl sulfoxide (DMSO), artemisinin, and cisplatin groups, captured at the end of the 21-day treatment period. Scale bar = 5 mm. (D) Weights of tumors harvested posttreatment. (E) Changes in body weight of mice in the Cal27 xenograft mouse model following treatment with DMSO, artemisinin, or cisplatin. Data are presented as means \pm standard deviation (SD) for n = 5 per group. Statistical significance compared to the control group is indicated as *p < .05, **p < .01, and ***p < .001.

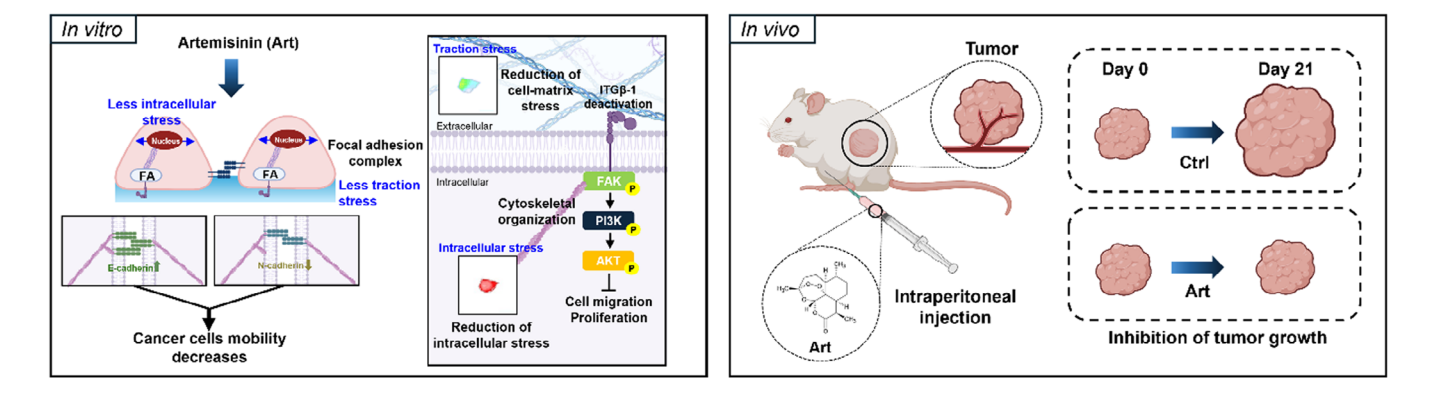


FIGURE 7 Schematic summary of the findings from this study and the proposed underlying molecular mechanism. Artemisinin demonstrates anticancer effects against tongue cancer both in vivo and in vitro by inhibiting cellular interactions and signaling pathways.

Taken together, our findings indicate that reducing substrate stiffness and artemisinin treatment effectively alleviate cell-ECM stress (traction stress), cell-cell stress (IS), and stress anisotropy (maximum intracellular shear stress), thereby curtailing cell mobility (Figure 7). These findings support the notion that lower substrate stiffness and artemisinin treatment mitigate cell-cell and IS, consequently impeding cell migration.

3 | CONCLUSIONS

This study elucidates how interactions among cells and underlying matrix dictate cellular behaviors. We demonstrated that the rigid TME fosters heightened cell-matrix adhesion, thus leading to elevated stress and tension and eventually increased cell spreading. Collectively, enhanced cell-cell interactions among these cells further

facilitate forward migration. Although our investigation did not address the disequilibrium of stress signals across monolayers, future studies are warranted to examine this phenomenon. It is well established that stress production varies heterogeneously across monolayers, with cells behind the leading edge experiencing higher stress levels, thus contributing to leading edge formation. Furthermore, our findings underscore the potential of artemisinin as an anticancer agent. Our findings provide evidence that artemisinin attenuates cellular proliferation and inhibits the downstream integrin-mediated FA pathway. This inhibition, coupled with reduced cell-matrix and cell-cell stress and tension, modulates cellular migratory behavior. Although our results need validation in preclinical and clinical models, we provide a strong proof-of-concept for the potential utility of artemisinin in the prevention and treatment of oral cancer metastasis.

4 | EXPERIMENTAL SECTION

4.1 | Cell culture and artemisinin treatment

Cal27 cells were obtained from the American Type Culture Collection (ATCC). The cells were cultured in high-glucose Dulbecco's Modified Eagle Medium (DMEM, cat# 11-965-092, Corning), supplemented with 10% fetal bovine serum (FBS, cat# 35-015-CV, Corning), and 1% penicillin-streptomycin (cat# 15140122, Corning), and maintained in an incubator at 37°C with 5% $\rm CO_2$. Artemisinin (cat# 361593, Sigma-Aldrich) was dissolved in DMSO (cat# D4540, Sigma-Aldrich) to prepare a 100 mM stock solution, which was then filtered using a syringe filter. Cell treatment was performed by diluting 50 μ M artemisinin from the stock in culture media. For the control group, cells were treated with a corresponding amount of DMSO diluted in growth media.

4.2 | Cell viability and proliferation assay

For the Live/Dead cell viability assay, 95% confluent cells were exposed to growth media containing either artemisinin or DMSO for 4 h. Subsequently, the Live/Dead Viability/Cytotoxicity Kit (cat# 3L-3224, Invitrogen), comprising 2 μM calcein AM and 4 μM ethidium homodimer-1 in phosphate-buffered saline (PBS) solution, was added to each well to replace the media, followed by a 30-min incubation at room temperature. Cell viability was assessed using ImageJ software (RRID:SCR_003070) by calculating the percentage of green-stained live cells relative to the total cell count.

To evaluate the proliferative capacity of Cal27 cells, $1 \times 10^4/\text{cm}^2$ cells were seeded and cultured for 72 h in media supplemented with artemisinin or DMSO. Media were replenished daily. The proliferation assay employed 3-(4,5-dimethylthiazol-2-yl)-2,5-diphenyltetrazolium bromide (MTT, cat# M6494, Invitrogen) and followed the manufacturer's instructions, with measurements taken at 24-h intervals. Optical density (OD) values were measured at 570 nm using a microplate reader. The proliferation rate was plotted as a relative fold change in OD values at each time point compared to the 0-h time point. Images were captured using an EVOS fluorescence microscope (M5000, Thermo Fisher Scientific) equipped with a 20× objective lens (N.A. = 0.45, cat# AMEP4924, EVOS, Thermo Fisher Scientific).

4.3 | Cell cycle and flow cytometry analyses

After 48 h of artemisinin treatment, cells were detached using trypsin-EDTA (cat# 25200056, Thermo Fisher Scientific) and rinsed once with PBS. Subsequently, 1×10^6 cells were fixed with 70% cold ethanol at 4°C overnight. After fixation, cells were washed with PBS and their concentration was adjusted to 1×10^6 cells/mL using PBS. The cells were permeabilized using 0.1% v/v Triton X-100 (cat# TRX777.500, BioShop) with 1% w/v bovine serum albumin (BSA, cat# SM-BOV-100, Geneall) in PBS for 15 min at 37°C, followed by a single wash with PBS. Subsequently, the cells were pelleted by centrifugation, resuspended, and incubated with 1 µL FxCycle Violet stain (cat# F10347, Thermo Fisher Scientific) per tube, thoroughly mixed, and then incubated in the dark at 2-6°C for 30 min according to the manufacturer's instructions. Samples were subjected to propidium iodide staining followed by FACS analysis (FACS Canto II, Becton Dickinson and Company) at Soonchunhyang Biomedical Research Core-Facility of the Korea Basic Science Institute (KBSI), with excitation at 450 nm and emission collected through a 450/50 bandpass filter.

4.4 | Colony formation assay

Cal27 cells were seeded into 6-well plates (500 cells/well) and cultured in DMEM supplemented with 10% FBS and 1% penicillin-streptomycin, with either artemisinin dissolved in DMSO (Art group) or DMSO alone (Ctrl group). The media were replenished daily, and the plates were incubated for 14 days in a 5% CO₂ incubator at 37°C. Subsequently, the cells were fixed with 4% paraformaldehyde (PFA, cat# SM-P01-100, Geneall) at room temperature for

20 min and stained with a 0.05% crystal violet solution (cat# C0775, Sigma-Aldrich) for 25 min at room temperature. The colony formation was quantified based on the number of colonies in each well using ImageJ software (RRID:SCR_003070).

4.5 □ Transwell migration and invasion assays

Transwell migration and invasion assays were conducted using Transwell inserts with polycarbonate membranes of 8.0 µm pore size (cat# 3422, Corning). For the migration assay, 200 μ L of a cell suspension containing 5 \times 10⁴ cells in growth media with 2% FBS and either DMSO or artemisinin was loaded into each upper chamber of the Transwell. In the Transwell invasion assay, the upper chamber was precoated with 40 µL Corning Matrigel Growth Factor Reduced Basement Membrane Matrix (cat# 356230, Corning), diluted in blank DMEM at a 1:3 v/v ratio. Subsequently, 700 µL growth media with 20% FBS was added to the bottom chamber to induce cell migration from the upper to the lower chamber. After 24 h (for invasion) and 12 h (for migration) incubation, the media were aspirated, and cells were fixed with 100% cold methanol and stained with 0.5% crystal violet for 15 min, respectively. Cell images were captured using an EVOS fluorescence microscope (Thermo Fisher Scientific) equipped with a 20x objective lens (N.A. = 0.45, cat# AMEP4924, EVOS, Thermo Fisher Scientific). The migrated and invaded areas were then quantified using ImageJ (RRID:SCR 003070) and plotted based on the percentage of the area covered with cells.

4.6 ■ Wound-healing assay

To investigate the impact of artemisinin on cell movement, wound-healing assays were conducted. Initially, 1×10^5 cells were seeded in each well of a silicone gasket (cat# 80206, ibidi) in growth media containing either artemisinin or DMSO. Once the cells had adhered adequately (approximately 8 h), the silicone gasket was removed, and images were captured using an EVOS fluorescence microscope (Thermo Fisher Scientific) equipped with a $10\times$ objective lens (N.A. = 0.3, cat# AMEP4623, EVOS, Thermo Fisher Scientific) at 12-h intervals. The image pixel size was $0.617\,\mu\text{m/pixel}$. The area of the wound gap was determined using MATLAB (MathWorks). The migration rate was plotted based on the area of the wound gap at each time point relative to the initial time point. Wound recovery was plotted by subtracting the area of the

wound gap at each time point from the wound gap area at 12 h prior.

4.7 | TCGA in silico analysis

The genetic status and expression of FAK and ITG β 1 encoding genes, coupled with overall survival data, were analyzed using the provisional dataset from "TCGA PanCancer Atlas" for HNSCC.⁶⁶ This dataset was accessed through cBioPortal (cbioportal.org). To compare gene expression between normal and cancerous tissues, expression data were sourced from TCGA HNSC cohort dataset (ID: TCGA.HNSC.sampleMap/HiSeqV2), available via UCSC Xena (xenabrowser.net).⁶⁷ Kaplan–Meier plots were generated to illustrate differences in patient survival based on the expression of FAK and ITG β 1. The statistical significance of any differences was assessed using the log-rank test.

4.8 | Immunohistochemical analysis

Human normal and tongue cancer tissues were obtained from patients with HNSC according to a protocol approved by the Institutional Review Board of Soonchunhyang University Cheonan Hospital (SCH IRB #2019-07-040) and processed for immunohistochemistry. Tongue normal tissues from HNSCC patients and tongue cancer tissues were fixed in 4% PFA, paraffin-embedded, and sectioned into 5μm slices. Sections were deparaffinized overnight in a 40°C dry incubator and subjected to two rounds of xylene treatment, followed by rehydration by passing through a series of graded ethanol solutions (100%, 95%, 80%, and 70%). After dewaxing and rehydration, sections were washed with distilled water. Endogenous peroxidase activity was blocked by treatment with 3% hydrogen peroxide (H₂O₂) for 10 min. Subsequently, a nonspecific protein blocking step was performed using 1% w/v BSA in PBS with 0.1% v/v Tween-20 (cat# P1379, Sigma-Aldrich). Subsequently, samples were incubated overnight with anti-alpha smooth muscle actin (α -SMA) (1:500) (cat# AB32575, Abcam), anti-FAK (1:250) (cat# AB40794, Abcam), and anti-ITGβ1 (1:100) (cat# SC-374429, Santa Cruz Biotechnology) antibodies at 4°C. Next, samples were incubated with polyclonal secondary antibodies, followed by incubation with streptavidin horseradish peroxidase (cat# 34002, Abcam). Immunoreactive staining was developed using 3,3'-diaminobenzidine according to the manufacturer's instructions (cat# 34002, Abcam), and coverslips were mounted using Cytoseal permanent mounting media. Positive staining was analyzed using the EVOS M700 imaging system (Thermo Fisher Scientific) with a 20x objective

lens (N.A. = 0.45, cat# AMEP4924, EVOS, Thermo Fisher Scientific).

4.9 | Immunofluorescence staining

Human normal tissue and tongue cancer tissue, fixed and harvested from an HNSC patient, were incubated overnight with a 20% w/v sucrose solution and subsequently embedded in optimal cutting temperature (cat# 4583, Sakura Finetek USA Inc.). The embedded samples were then sectioned into 6 µm-thick slices using a cryostat (Leica) at the Soonchunhyang Biomedical Research Core-Facility of the KBSI. Sections were treated with 0.5% Triton X-100 solution for 10 min followed by three 5-min washes with PBS. Subsequently, sections were incubated in a solution of 1% BSA with 0.05% Tween 20 for 30 min at room temperature. For immunofluorescence staining, cryosections were incubated with primary antibody for 1 h at room temperature. After washing with PBS, the sections were incubated with a fluorescence-conjugated secondary antibody for 1 h at room temperature. The antibodies used are listed in Table S1. Imaging was conducted using a fluorescence microscope EVOS M700 imaging system (Thermo Fisher Scientific) equipped with a 20× objective lens (N.A. = 0.45, cat# AMEP4924, EVOS, Thermo Fisher Scientific).

4.10 | Nanoindentation

To measure cell stiffness, both soft (2.55 kPa) and stiff (49.4 kPa) PAA gels were prepared on hydrophilic cover glass (dia. = 18 mm). To ensure the gel attachment to the cover glass, the cover glass was treated with a mixture of 3-trimethoxysilylpropylmethacrylate (cat# 440159, Sigma-Aldrich), acetic acid (cat# 1005-4105, Daejung Chemicals), and ethanol for 5 min. Cal27 cells were seeded onto gels, and the cover glass was then securely fixed to the bottom of a 6-well plate to ensure a stable environment for accurate measurement of the stiffness of cells. Cells were subjected to nanoindentation at 37°C in the presence of media. Nanoindentation was conducted using the Pavone Nanoindenter (Optics11 Life), following the manufacturer's instructions. For cell samples, single cells were randomly selected for measurement.

4.11 | Quantitative real-time PCR

Cal27 cells were cultured in the absence or presence of 50 μ M artemisinin for 24 h. Total RNA was extracted from cultured cells using TRIzol Reagent (cat# 15596018, Invitrogen), following the manufacturer's protocol. Sub-

sequently, the isolated RNA was reverse-transcribed using ReverTra Ace qPCR RT Master Mix (cat# FSQ-301, TOYOBO), as per the manufacturer's instructions. Quantitative real-time PCR assays were performed on a QuantStudio 1 Real-Time PCR System (Applied Biosystems). Each qPCR amplification was performed in triplicate using SYBR Green Realtime PCR Master Mix (cat# F0924K, TOYOBO) along with the primers listed in Table S2. Data were analyzed using the $\Delta\Delta$ Ct method, with 18S ribosomal RNA serving as an internal reference. Any change in the expression of the gene of interest was normalized to the control sample. The results of qPCR analyses were graphed, with the *y*-axis denoting the fold change in gene expression.

4.12 | Immunoblotting analysis

Cal27 cells were cultured in the absence or presence of 50 µM artemisinin for 24 h. Whole-cell lysates were prepared using RIPA buffer (cat# EBA11491, Elpis Biotech), supplemented with protease and phosphatase inhibitors (Sigma-Aldrich). The protein concentrations of the lysates were quantified using the Pierce BCA Protein Assay Kit (cat# 23225, Thermo Fisher Scientific). Equal amounts of protein from each sample were subjected to SDS-PAGE for separation. Subsequently, proteins were transferred from the gel to polyvinylidene difluoride membranes (Pall Corporation). The membranes were blocked in 5% skim milk (cat# SKI400.500, BioShop) in Tris-buffered saline containing 0.1% Tween 20 (cat# P1379-100ML, Sigma-Aldrich) (TBST) for 1 h at room temperature, followed by overnight incubation at 4°C with primary antibodies at the manufacturer's recommended concentrations. After washing with TBST, the membranes were incubated with appropriate secondary antibodies at room temperature for 1 h, according to the manufacturer's instructions. Finally, the membranes were washed with TBST, and immunoreactive bands were imaged using an Amersham imager 600 (GE Healthcare) and Amersham ECL Prime detection reagent (cat# RPN2235, Cytiva). The intensity of each band was quantified using ImageJ software (Image J, RRID:SCR_003070). For detailed information on the antibodies used, please see Table S3; original, uncropped, and unadjusted raw images of all western blots used in this study are provided in Figure S3.

4.13 | Hematoxylin and eosin staining

Tissue specimens were fixed with 4% PFA in PBS for 24 h, followed by gradual dehydration in ethanol and embedding in paraffin overnight. Tissue paraffin blocks were sectioned at $5 \mu m$ thickness. After deparaffinization

in S3-Histo xylene substitute (cat# 4322, BBC Biochemical), the samples were initially stained for nuclei using hematoxylin (Mayer's modified, cat# AB220365, Abcam) for 4 min and rinsed several times with water to remove excess stain. Subsequently, the samples were immersed multiple times in 1% v/v acid ethanol for destaining. Next, specimens were stained with eosin (cat# HT110216, Sigma-Aldrich) for 8 min, dehydrated in a series of graded ethanol, and treated with xylene. Finally, the hematoxylin and eosin–stained specimens were dehydrated in ethyl alcohol and mounted for visualization and photography. All images were captured using a fluorescence microscope EVOS M700 imaging system (Thermo Fisher Scientific).

4.14 | Masson's trichrome staining

Sample slices for Masson's trichrome (MT) staining were processed using the MT staining kit (cat# BAQ086, G Biosciences), following the manufacturer's protocol. Following deparaffinization, sample slices were immersed in Weigert's iron hematoxylin solution for 5 min. Subsequently, samples were washed with tap water for 10 min and were then placed in a Biebrich scarlet solution for 3 min, followed by immersion in 3% phosphomolybdic—phosphotungstic acid for 2 min, and an aniline blue solution for 5 min. The slices were rinsed with tap water and then immersed in 1% v/v acetic acid for 1 min. Finally, the slices were washed with tap water, dehydrated, and mounted for visualization and photography.

4.15 | Cell morphology analysis

Following the seeding of cells at a density of $5 \times 10^4/\text{cm}^2$ and culturing them in media with or without artemisinin for 24 h, cells were stained with green cell tracker (cat# C7025, Invitrogen) for 45 min before image acquisition. Images were captured using a confocal microscope (LSM 710; Carl Zeiss) at the Soonchunhyang Biomedical Research Core Facility of the KBSI, employing a 40× objective lens with a $0.6 \times$ zoom out (N.A. = 1.2, $40 \times$ C-Apochromat 40×/1.2 Korr M27, Zeiss). The pixel size was 0.17 µm/pixel. As reported earlier, 68 MATLAB-coded image-processing algorithms were utilized for morphological analysis, encompassing measurements of area, major axis, minor axis, and circularity. Cell images were subjected to binarization via histogram-based threshold algorithms (HTA).^{68a} The area was quantified as the number of pixels within the cell and converted to micrometers by multiplying by the pixel size. The major and minor axes were determined through the eigenvalue analysis of second-order image moment analysis. 68b Circularity was calculated as the squared ratio between the perimeter length of a cell and that of a perfect circle $(4\pi A/P^2)$; where A = cell area and P = cellular perimeter length).

4.16 | Preparation of PAA gel

To replicate the physical properties of native tongue tissue, as previously investigated, 47,69 we prepared soft (2.55 kPa, AA/Bis = 4%/0.15%) and rigid (49.4 kPa,AA/Bis = 10%/0.30%) PAA hydrogels on glass-bottom dishes (cat# 101350, SPL) following established protocols.⁷⁰ PAA solutions with varying final concentrations were prepared according to previously published methods.71 In brief, the glass-bottom dish was rendered hydrophilic by exposing the glass surface to a Bunsen burner flame and treating it with sodium hydroxide (0.1 M, cat# 39155S0350). Glass activation involved the addition of 3aminopropyl trimethoxysilane (Silane, cat# 28177-500ML, Sigma-Aldrich) and glutaraldehyde (0.5%; cat# G5882, Sigma-Aldrich). For cellular force measurement, red fluorescent beads (0.01%, ex/em = 580/605 nm; dia. = 0.5 μ m (40 \times magnification); cat# F8812, dia. = 1.0 μ m (10 \times magnification); cat# F8821, Invitrogen) were vortexed and embedded in the PAA solution. Gel polymerization was initiated by the addition of ammonium persulfate (0.6% w/v in DI water; cat# AMP001, BioShop) and N,N,N',N'-tetramethylethylenediamine (0.4% v/v in DI water; cat# TEM001, BioShop), and the gels were sandwiched between activated glass and an inactive 18mm glass coverslip (cat# 0111580, Marienfeld). After 1 h polymerization, the inactive coverslip was removed. To promote cell attachment, collagen type I (100 µg/mL; cat# 354236, Corning) was conjugated on the substrate with the bifunctional cross-linker N-sulfosuccinimidyl-6-[4'azido-2'-nitrophenylamino] hexanoate (Sulfo-SANPAH, 0.5 mg/mL, cat# 22589, Thermo Scientific) using UV light (365 nm; Blak-Ray XX-15L, cat# UVP95004206). Subsequently, the gels were sterilized under UV light (254 nm; Mineralight XX-15S, cat# 95004209) for 10 min and preconditioned by equilibrating them with cell culture medium at 37°C in a 5% CO_2 environment for a minimum of 10 min before cell seeding.

4.17 | Analysis of cell-ECM forces using traction force microscopy

TFM measurements were conducted on cells seeded at a density of $5 \times 10^4/\text{cm}^2$ onto PAA gels of varying stiffness (2.55 and 49.4 kPa) in the absence and presence of 24 h artemisinin treatment. TFM analysis was based on the displacement of fluorescent beads embedded within the PAA

gels. Images of fluorescence beads, cells, and differential interference contrast (DIC) were acquired using a laser confocal microscope (LSM-710; Carl Zeiss) equipped with a $40 \times$ objective lens (C-Apochromat, NA = 1.2). The image pixel size was set at 0.42 µm/pixel. Bead displacements were calculated using the particle image velocimetry method in MATLAB (MathWorks) by comparing images in a null-force state (absence of cells) and a force state (presence of cells). 70a To achieve the null-force state, 1 mL of 10% w/v sodium lauryl sulfate (SDS, 196-08675, Wako Chemicals) and 1% v/v Triton X-100 (cat# TRX777.500, Bioshop) in distilled water was used to remove the cells. The finite element method (FEM) was employed to solve partial differential equations using Abaqus software (Dassault Systèmes). Subsequently, traction stress vectors in the x and y directions were derived from the stress tensor obtained through FEM analysis. Traction stress magnitude (TS_{mag} and stress; Equation 1) was defined as the average stress magnitude beneath the cell, calculated as the force divided by the cell's area. The vertical (TS_{vertical}; Equation 2) and horizontal (TS_{horizontal}; Equation 3) components of traction stresses were determined based on the relationship between the stress vector and the shape of wound edges (Figure 5A).

Traction stress magnitude:
$$TS_{mag} = \sqrt{\sigma_x^2 + \sigma_y^2} dx dy$$
 (1)

where $\sigma(x,y) = [\sigma_x, \sigma_y]$ is the traction stress vector.

4.18 | Quantification of focal adhesion (FA) and actin cytoskeleton

FA images were captured from cells cultured on gel substrates in media with or without artemisinin. Cells were seeded at a density of $5 \times 10^4/\text{cm}^2$ as seeding density and, after 24 h of culture, were fixed with 4% PFA (cat# CNP015-0500, CELLNEST) and permeabilized with 0.5% v/v Triton X-100. Subsequently, cells were blocked with 1% w/v BSA PBS containing 0.05% Tween 20, and then labeled with phospho-FAK (Tyr397, 1:400, cat# AB81298, Abcam) as the primary antibody, followed by counterstaining with anti-rabbit 488 antibody (1:400, cat# RSA1241, Bioacts). Additionally, F-actin was labeled using Alexa Fluor 488 Phalloidin (1:400, cat# A12379, Invitrogen), and Hoescht (1:1000) was used for nuclear staining, all for 1 h, followed by PBS washing. The details of the antibodies are listed in Table S1. Cell images were captured using a fluorescence microscope (EVOS M7000, Thermo Fisher Scientific) equipped with a 20× objective lens (N.A. = 0.45, cat# AMEP4924, EVOS, Thermo Fisher Scientific). The pixel size of the images was 0.31 µm/pixel. Images were analyzed using a custom MATLAB program (MathWorks) to mini-

mize subjective determination of threshold values, thereby reducing variability and experimental errors, as detailed in a previous study.^{68a} Briefly, HTA involved the following steps: (1) background noise elimination by subtracting 0.5% of the minimum values in the image histogram. (2) Drawing a region of interest to confine cell analysis. (3) Determining the absolute threshold using a combination of mean (m) and standard deviation (SD) (σ) of intensity, along with a relative threshold value (α), where approximately 5% of maximum intensity was used as a threshold. (4) Applying minimum and maximum size filters of 1.5 and 30 µm², respectively, to eliminate noise from protein fragments and aggregates. Following binarization using HTA, morphological and intensity parameters of FAs were extracted. These parameters included area, centroid, maximum axis length, elongation, and circularity of individual FAs, following the method described for cellular morphology analysis. Total intensity was obtained by summing pixel values within FA boundaries, and mean intensity was calculated by dividing the total intensity by the FA area. For improved visualization, images were reacquired using a laser confocal microscope (LSM-710; Carl Zeiss) equipped with a 40x objective lens (C-Apochromat, NA = 1.2). The pixel size of the images was $0.42 \, \mu m/pixel.$

4.19 | Single-cell tracking analysis

To evaluate the migration trajectories of individual cells following artemisinin treatment, cells were seeded at a density of $5 \times 10^4/\text{cm}^2$ and allowed to settle for 1 h before the commencement of the experiment. After a single-PBS wash, the medium was replaced with fresh medium containing either artemisinin or DMSO. Real-time imaging was conducted using the EVOS M700 imaging system (Thermo Fisher Scientific) equipped with a $20\times$ objective lens (N.A. = 0.45, cat# AMEP4924, EVOS, Thermo Fisher Scientific). The pixel size was set at 0.31 µm/pixel. Images were captured over a 12-h period, with 5-min intervals between each capture. Automatic tracking was conducted utilizing TrackMate in FIJI, employing the LoG spot detector and Simple Lap tracker for spot tracking. ⁷²

4.20 | Analysis of intracellular stress using monolayer stress microscopy (MSM)

IS for collective cells were quantified using MSM, as per established methodologies. Similar to the conventional wound healing assay, 1×10^5 cells were seeded into each well of a silicone gasket (cat# 80206, ibid) in growth media

containing either artemisinin or DMSO. After 8 h, the silicone gasket was removed to create a wound gap (0 h). Cell migration was monitored and stopped at 12 h postgasket removal. Images were acquired for analysis. Images of fluorescence beads, cells, and DIC were acquired using a laser confocal microscope (LSM-710; Carl Zeiss) equipped with a 10× objective lens (C-Apochromat, NA = 0.45, 0.6× zoom out), with a pixel size of 0.69 $\mu m/pixel$. Briefly, the highest (τ_{max}) and lowest (τ_{min}) stress levels were determined via eigenvalue analysis of the IS tensor. These values were then utilized to calculate stress magnitude (IS $_{mag}$; Equation 2) and maximum shear IS (IS $_{maxshear}$; Equation 3).

Intracellular stress magnitude :
$$IS_{mag} = \sqrt{\tau_{max}^2 + \tau_{min}^2}$$
 (2)

Maximum shear stress:
$$IS_{maxshear} = 0.5 \times (\tau_{max} - \tau_{min})$$
 (3)

where τ_{max} and τ_{min} represent the maximum and minimum IS determined through eigenvalue analysis of the stress tensor, respectively.

4.21 | Cal27 xenograft mouse model

All animal studies were approved by the Institutional Animal Care and Use Committee (IACUC) at Soonchunhyang University (protocol number: SCH22-0011). Immunedeficient NSG (NOD scid gamma) mice, aged over 33 weeks and of both sexes, were bred in-house and used to evaluate the in vivo efficacy of artemisinin. Prior to surgical procedures, mice were anesthetized using isoflurane (2%–3% in oxygen, cat# 657801261, Hana Pharm Co.) administered via inhalation, with the anesthesia maintained throughout the procedure. For the xenograft studies, Cal27 cells were cultured in DMEM medium supplemented with 10% FBS (cat# 35-015-CV, Corning) and 1% penicillin/streptomycin (cat# 15140122, Corning), at 37°C in a humidified 5% CO2 incubator. For cell transplantation, 1×10^6 cells were suspended in a 1:1 (v/v) mixture of DMEM and Matrigel (cat# 354234, Corning) at a concentration of 1×10^6 cells/100 µL.⁷⁴ The cell suspension was subcutaneously injected into both flanks of each mouse. Mice were housed under specific pathogen-free conditions and acclimated before the start of the experiment. Once the tumor volume reached at least 100 mm³, the mice were randomized into three treatment groups (n = 5 per group) as follows:

1. DMSO (vehicle control): Mice were treated with DMSO (cat# D4540, Sigma-Aldrich) as a vehicle at a dose of 4 μ L/g body weight, administered daily via intraperitoneal injection.

- 2. Artemisinin: Mice received artemisinin (50 μ g/g body weight, cat# 361593, Sigma-Aldrich) administered daily via intraperitoneal injection.
- 3. Cisplatin (positive control): Mice were treated with cisplatin (5 μg/g body weight, cat# ab141398, Abcam) administered twice weekly via intraperitoneal injection.

Tumor volume was measured using digital calipers and the body weight were recorded weekly for up to 21 days.⁷⁵ Tumor volumes were calculated using the following formula⁷⁶:

Tumor volume $(mm^3) = \frac{1}{2} \times long axis \times short axis^2$ (4)

4.22 | Statistical analysis

Data were statistically analyzed using Graph Pad Prism v.10 (Graph Pad Software Inc.). The graphs were constructed to represent mean values, with error bars indicating the standard error of the mean. For the in vivo data, the data were shown as mean \pm SD. The statistical significance of differences observed in bar graphs was determined using Student's t-test for comparisons between two groups, and one-way analysis of variance followed by Tukey's post-hoc analysis for comparisons among multiple groups. For mechanical stress data, including TFM and MSM, violin plots were generated to depict the median and quartiles, with statistical comparisons performed using the non-parametric Kruskal-Wallis test followed by Dunn's test for post-hoc analysis. Statistical significance was indicated by asterisks as follows: p < .05, p < .01, and****p* < .001.

AUTHOR CONTRIBUTIONS

Laurensia Danis Anggradita: Conceptualization; methodology; investigation; formal analysis; writing original draft; writing-review and editing. Joo Hyun Kim: Methodology; investigation; formal analysis. Min-**Kyu Kim**: Methodology; investigation; formal analysis. Ji Won Son: Methodology; investigation; formal analysis. Mohd Farhan: Methodology; investigation; formal analysis. Jothilin Subitsha Alex Jeberson: Methodology; investigation; formal analysis. Ali Taghizadeh: Methodology; investigation; formal analysis. Hae-Won Kim: Methodology; investigation; formal analysis. Jae Hong Park: Methodology; investigation; formal analysis. Jaemoon Yang: Methodology; investigation; formal analysis. Hyung Kwon Byeon: Methodology; investigation; formal analysis. Sung Sik Hur: Investigation; formal analysis; writing-original draft; writing-review and editing; funding acquisition. Myung Jin Ban: Conceptualization; methodology; investigation; formal analysis;

writing—original draft; writing—review and editing; funding acquisition. **Yongsung Hwang**: Conceptualization; methodology; investigation; formal analysis; writing—original draft; writing—review and editing; funding acquisition.

ACKNOWLEDGMENTS

This work was supported by the Soonchunhyang University Research Fund and the National Research Foundation of Korea funded by the Ministry of Science and ICT (MSIT) [grant numbers: 2019R1A5A8083404, RS-2022-NR075792, RS-2023-00284258, RS-2024-00440151, RS-2024-00348582, 2021R1A5A2022318, and 2019R1I1A3A01063629].

CONFLICT OF INTEREST STATEMENT

The authors declare no conflict of interest.

DATA AVAILABILITY STATEMENT

The data that support the findings of this study are available in the Supporting Information section of this article.

ORCID

Laurensia Danis Anggradita https://orcid.org/0009-0003-3120-601X

Joo Hyun Kim https://orcid.org/0000-0002-3279-2474

Min-Kyu Kim https://orcid.org/0009-0008-7203-1603

Sung Sik Hur https://orcid.org/0000-0003-4211-0497

Myung Jin Ban https://orcid.org/0000-0003-2069-2422

Yongsung Hwang https://orcid.org/0000-0001-5558-5171

REFERENCES

- M. Badwelan, H. Muaddi, A. Ahmed, K. T. Lee, S. D. Tran, Curr. Oncol. 2023, 30, 3721.
- a) N. W. Johnson, P. Jayasekara, A. A. H. K. Amarasinghe, *Periodontology 2000* **2011**, *57*, 19. b) F. R. Pires, A. B. Ramos, J. B. Oliveira, A. S. Tavares, P. S. Luz, T. C. Santos, *J. Appl. Oral. Sci.* **2013**, *21*, 460.
- 3. A. Bugshan, I. Farooq, F1000Research 2020, 9, 229.
- 4. S. Saraf, S. PK, R. K. Das, Oral Oncology Reports 2023, 5, 100016.
- P. Jayanthi, B. R. Varun, J. Selvaraj, J. Oral Maxillofac. Pathol. 2020, 24, 189.
- B. F. Matte, A. Kumar, J. K. Placone, V. G. Zanella, M. D. Martins, A. J. Engler, M. L. Lamers, J. Cell Sci. 2019, 132, jcs224360.
- 7. B. Peltanova, M. Raudenska, M. Masarik, *Mol. Cancer* **2019**, *18*, 63.
- 8. S. Y. Moon, P. S. de Campos, B. F. Matte, J. K. Placone, V. l. G. Zanella, M. D. Martins, M. L. Lamers, A. J. Engler, *Mol. Biol. Cell* **2023**, *34*, ar89.
- K. A. Jansen, P. Atherton, C. Ballestrem, Semin. Cell Dev. Biol. 2017, 71, 75.
- C. S. Chen, J. L. Alonso, E. Ostuni, G. M. Whitesides, D. E. Ingber, *Biochem. Biophys. Res. Commun.* 2003, 307, 355.
- X. G. Jiang, P. F. Austin, R. A. Niederhoff, S. R. Manson, J. J. Riehm, B. L. Cook, G. Pengue, K. Chitaley, K. Nakayama, K. I. Nakayama, S. J. Weintraub, Mol. Cell Biol. 2009, 29, 5104.

- A. J. Engler, S. Sen, H. L. Sweeney, D. E. Discher, Cell 2006, 126, 677
- J. L. Leight, M. A. Wozniak, S. Chen, M. L. Lynch, C. S. Chen, Mol. Biol. Cell 2012, 23, 781.
- 14. A. K. Harris, D. Stopak, P. Wild, Nature 1981, 290, 249.
- S. S. Hur, J. H. Jeong, M. J. Ban, J. H. Park, J. K. Yoon, Y. Hwang, BMB Rep. 2020, 53, 74.
- a) N. Zuela-Sopilniak, J. Lammerding, *Philos. Trans. R. Soc., B* 2019, *374*, 20180219.
 b) D. N. Clarke, A. C. Martin, *Curr. Biol.* 2021, *31*, R667.
- 17. D. T. Tambe, C. C. Hardin, T. E. Angelini, K. Rajendran, C. Y. Park, X. Serra-Picamal, E. H. Zhou, M. H. Zaman, J. P. Butler, D. A. Weitz, J. J. Fredberg, X. Trepat, *Nat. Mater.* **2011**, *10*, 469.
- S. S. Hur, J. C. del Álamo, J. S. Park, Y.-S. Li, H. A. Nguyen, D. Teng, K.-C. Wang, L. Flores, B. Alonso-Latorre, J. C. Lasheras, S. Chien, *Proc. Natl. Acad. Sci.* 2012, 109, 11110.
- D. T. Tambe, U. Croutelle, X. Trepat, C. Y. Park, J. H. Kim, E. Millet, J. P. Butler, J. J. Fredberg, PLoS ONE 2013, 8, e55172.
- a) X. Trepat, M. R. Wasserman, T. E. Angelini, E. Millet, D. A. Weitz, J. P. Butler, J. J. Fredberg, *Nat. Phys.* **2009**, *5*, 426. b) N. S. Gov, *HFSP J.* **2009**, *3*, 223.
- a) X.-Z. Su, L. H. Miller, Sci. China Life Sci. 2015, 58, 1175. b) Y.
 Tu, Angew. Chem. Int. Ed. 2016, 55, 10210.
- C. Shi, H. Li, Y. Yang, L. Hou, Mediators Inflammation 2015, 2015, 435713.
- S. Zhu, W. Liu, X. Ke, J. Li, R. Hu, H. Cui, G. Song, Oncol. Rep. 2014, 32, 1094.
- R. Shi, H. Cui, Y. Bi, X. Huang, B. Song, C. Cheng, L. Zhang, J. Liu, C. He, F. Wang, *Oncol. Lett.* 2015, 9, 2249.
- Y. Augustin, H. M. Staines, S. Krishna, *Pharmacol. Ther.* **2020**, 216, 107706.
- W. Liang, J. Liu, H. Wu, X. Qiao, X. Lu, Y. Liu, H. Zhu, L. Ma, Oncol. Lett. 2019, 18, 3407.
- M. Farhan, M. Silva, X. Xingan, Z. Zhou, W. Zheng, Oxid. Med. Cell. Long. 2021, 2021, 9911537.
- a) X. H. Yu, J. B. Wu, H. Y. Fan, L. Dai, H. C. Xian, B. J. Chen, P. Liao, M. C. Huang, X. Pang, M. Zhang, X. H. Liang, Y. L. Tang, Oral Dis. 2024, 30, 363. b) S. Zheng, R. Wu, Y. Deng, Q. Zhang, Bioengineered 2022, 13, 227. c) S. Shi, H. Luo, Y. Ji, H. Ouyang, Z. Wang, X. Wang, R. Hu, L. Wang, Y. Wang, J. Xia, B. Cheng, B. Bao, X. Li, G. Liao, B. Xu, Oxid. Med. Cell. Long. 2023, 2023, 9595201.
- A. M. Posadino, R. Giordo, G. Pintus, S. A. Mohammed, I. E. Orhan, P. V. T. Fokou, F. Sharopov, C. O. Adetunji, Z. Gulsunoglu-Konuskan, A. Ydyrys, *Biomed. Pharmacother.* 2023, 163, 114866.
- X. Feng, L. Li, H. Jiang, K. Jiang, Y. Jin, J. Zheng, *Biochem. Biophys. Res. Commun.* 2014, 444, 376.
- 31. H.-J. Zhou, J.-L. Zhang, A. Li, Z. Wang, X.-E. Lou, Cancer Chemother Pharmacol. 2010, 66, 21.
- Y. Zhou, X. Wang, J. Zhang, A. He, Y. L. Wang, K. Han, Y. Su, J. Yin, X. Lv, H. Hu, *Oncotarget* 2017, 8, 18260.
- 33. P. Xiao, Q. Liang, Q. Chen, H. Liu, Acta Biochim. Pol. 2022.
- B. Zhang, Z. Zhang, J. Wang, B. Yang, Y. Zhao, Z. Rao, J. Gao, Oncol. Lett. 2018, 15, 7531.
- H. Yamaguchi, J. Wyckoff, J. Condeelis, Curr. Opin. Cell Biol. 2005, 17, 559.
- K. Kumari, S. Keshari, D. Sengupta, S. C. Sabat, S. K. Mishra, *BMC Cancer* 2017, 17, 858.

- D. Nandi, P. S. Cheema, A. Singal, H. Bharti, A. Nag, Front. Oncol. 2021, 11, 751271.
- a) P. Friedl, K. Wolf, Nat. Rev. Cancer 2003, 3, 362. b) J. S. Wu, J. Jiang, B. J. Chen, K. Wang, Y. L. Tang, X. H. Liang, Transl. Oncol. 2021, 14, 100899.
- Z. Xu, L. Zou, G. Ma, X. Wu, F. Huang, T. Feng, S. Li, Q. Lin, X. He, Z. Liu, X. Cao, Am. J. Cancer Res. 2017, 7, 531.
- 40. P. Costa, J. Scales Tm Fau Ivaska, M. Ivaska J Fau Parsons, M. Parsons, *PLoS ONE* **2013**, *8*, e74659.
- 41. L. Zhang, W. Zou, Mol. Med. Rep. 2015, 12, 7869.
- 42. a) A. Tadijan, J. D. Humphries, I. Samaržija, N. Stojanović, J. Zha, K. Čuljak, M. Tomić, M. Paradžik, D. Nestić, H. Kang, M. J. Humphries, A. Ambriović-Ristov, *Front. Cell Dev. Biol.* 2021, 9, 786758. b) S. J. Park, H. J. Min, C. Yoon, S. H. Kim, J. H. Kim, S. Y. Lee, *Cell. Signalling* 2023, 110, 110808.
- 43. J. Cooper, F. G. Giancotti, Cancer Cell 2019, 35, 347.
- 44. J. J. Lee, R. A. H. van de Ven, E. Zaganjor, M. R. Ng, A. Barakat, J. J. P. G. Demmers, L. W. S. Finley, K. N. Gonzalez Herrera, Y. P. Hung, I. S. Harris, S. M. Jeong, G. Danuser, S. S. McAllister, M. C. Haigis, *Proc. Natl. Acad. Sci.* 2018, 115, 7057.
- 45. N. Kurio, T. Shimo, T. Fukazawa, T. Okui, N. M. M. Hassan, T. Honami, Y. Horikiri, S. Hatakeyama, M. Takaoka, Y. Naomoto, A. Sasaki, *Oral Oncol.* **2012**, *48*, 1159.
- 46. C. Y. Loh, J. Y. Chai, T. F. Tang, W. A.-O. Wong, G. Sethi, M. K. Shanmugam, P. A.-O. Chong, C. Y. Looi, *Cells* **2019**, *8*, 1118.
- 47. a) S. Cheng, M. Gandevia Sc Fau Green, R. Green M Fau Sinkus, L. E. Sinkus R Fau Bilston, L. E. Bilston, J. Biomech.
 2011, 44, 450. b) E. C. Brown, S. Cheng, D. K. McKenzie, J. E. Butler, S. C. Gandevia, L. E. Bilston, Sleep 2015, 38, 537.
- M. A.-O. Shibata, A. A.-O. Ishikawa, J. A.-O. Ishii, E. A.-O. Anzai, H. A.-O. Yagishita, T. A.-O. Izumo, J. A.-O. Sumino, M. A.-O. Katsurano, Y. A.-O. Kim, H. A.-O. Kanda, M. A.-O. Ushijima, K. A.-O. Yagihara, T. A.-O. Yoda, *Oral Radiol.* 2022, 38, 278.
- L. Jingyuan, L. Yu, J. Hong, W. Tao, L. Kan, L. Xiaomei, L. Guiqing, L. Yujie, *Transl. Oncol.* 2023, 33, 101681.
- 50. a) S. Tavares, A. F. Vieira, A. V. Taubenberger, M. Araújo, N. P. Martins, C. Brás-Pereira, A. Polónia, M. Herbig, C. Barreto, O. Otto, J. Cardoso, J. B. Pereira-Leal, J. Guck, J. Paredes, F. Janody, *Nat. Commun.* 2017, 8, 15237. b) J. Haynes, N. Srivastava J Fau Madson, T. Madson N Fau Wittmann, D. L. Wittmann T Fau Barber, D. L. Barber, *Mol. Biol. Cell* 2011, 22, 4750.
- a) Y.-L. Hu, S. Lu, K. W. Szeto, J. Sun, Y. Wang, J. C. Lasheras, S. Chien, Sci. Rep. 2014, 4, 6024. b) K. E. Michael, K. L. Dumbauld Dw Fau Burns, S. K. Burns Kl Fau Hanks, A. J. Hanks Sk Fau García, A. J. García, Mol. Biol. Cell 2009, 20, 2508.
- T. Yeung, P. C. Georges, L. A. Flanagan, B. Marg, M. Ortiz, M. Funaki, N. Zahir, W. Ming, V. Weaver, P. A. Janmey, *Cell Motil.* 2005, 60, 24.
- J. Schrader, T. T. gordon-Walker, R. L. Aucott, M. van Deemter,
 A. Quaas, S. Walsh, D. Benten, S. J. Forbes, R. G. Wells, J. P. Iredale, *Hepatology* 2011, 53, 1192.
- Y. Yu, L.-J. Ren, X.-Y. Liu, X.-B. Gong, W. Yao, Eur. J. Cell Biol. 2021, 100, 151178.
- A. K. Yip, K. Iwasaki, C. Ursekar, H. Machiyama, M. Saxena, H. Chen, I. Harada, K.-H. Chiam, Y. Sawada, *Biophys. J.* 2013, 104, 19.

- B. Pontes, P. Monzo, L. Gole, A.-L. Le Roux, A. J. Kosmalska, Z. Y. Tam, W. Luo, S. Kan, V. Viasnoff, P. Roca-Cusachs, L. Tucker-Kellogg, N. C. Gauthier, J. Cell Biol. 2017, 216, 2959.
- A. V. Murashko, A. A. Frolova, A. A. Akovantseva, S. L. Kotova,
 P. S. Timashev, Y. M. Efremov, *Biochim. Biophys. Acta Gen. Subj.* 2023, 1867, 130348.
- 58. P. Pisani, M. Airoldi, A. Allais, P. A. Valletti, M. Battista, M. Benazzo, R. Briatore, S. Cacciola, S. Cocuzza, A. Colombo, B. Conti, A. Costanzo, L. della Vecchia, N. Denaro, C. Fantozzi, D. Galizia, M. Garzaro, I. Genta, G. A. Iasi, M. Krengli, V. Landolfo, G. V. Lanza, M. Magnano, M. Mancuso, R. Maroldi, L. Masini, M. C. Merlano, M. Piemonte, S. Pisani, A. Prina-Mello, L. Prioglio, M. G. Rugiu, F. Scasso, A. Serra, G. Valente, M. Zannetti, A. Zigliani, Acta Otorhinolaryngo 2020, 40, S1.
- T. Wu, S. Xiong, M. Chen, B. T. Tam, W. Chen, K. Dong, Z. Ma,
 Z. Wang, G. Ouyang, *Matrix Biol.* 2023, 121, 22.
- A. Bajpai, J. Tong, W. Qian, Y. Peng, W. Chen, *Biophys. J.* 2019, 117, 1795.
- 61. G. Cai, A. Nguyen, Y. Bashirzadeh, S. S. Lin, D. Bi, A. P. Liu, Front. Cell Dev. Biol. 2022, 10, 933042.
- S. S. Chang, A. D. Rape, S. A. Wong, W. H. Guo, Y. L. Wang, *Mol. Biol. Cell* 2019, 30, 3104.
- M. P. Crespo-Ortiz, M. Q. Wei, BioMed Res. Int., 2012, 2012, 247597.
- 64. a) A. Orwick, S. M. Sears, C. N. Sharp, M. A. Doll, P. P. Shah, L. J. Beverly, L. J. Siskind, Am. J. Physiol. Renal Physiol. 2023, 324, F287. b) H. Kong, J. Yang, X. Wang, N. Mamat, G. Xie, J. Zhang, H. Zhao, J. Li, Int. J. Biol. Macromol. 2024, 265, 130706. c) M. A.-O. Perše, Biomedicines 2021, 9, 1406. d) Y. Tong, Y. Liu, H. Zheng, L. Zheng, W. Liu, J. Wu, R. Ou, G. Zhang, F. Li, M. Hu, Z. Liu, L. Lu, Oncotarget 2016, 7.
- X. Gao, X. Lin, Q. A.-O. Wang, J. A.-O. Chen, Med. Res. Rev. 2024, 44, 867.
- 66. J. Liu, T. Lichtenberg, K. A. Hoadley, L. M. Poisson, A. J. Lazar, A. D. Cherniack, A. J. Kovatich, C. C. Benz, D. A. Levine, A. V. Lee, L. Omberg, D. M. Wolf, C. D. Shriver, V. Thorsson, S. J. Caesar-Johnson, J. A. Demchok, I. Felau, M. Kasapi, M. L. Ferguson, C. M. Hutter, H. J. Sofia, R. Tarnuzzer, Z. Wang, L. Yang, J. C. Zenklusen, J. Zhang, S. Chudamani, J. Liu, L. Lolla, R. Naresh, et al., *Cell* 2018, 173, 400.
- 67. M. J. Goldman, B. Craft, M. Hastie, K. Repečka, F. McDade, A. Kamath, A. Banerjee, Y. Luo, D. Rogers, A. N. Brooks, J. Zhu, D. Haussler, *Nat. Biotechnol.* **2020**, *38*, 675.
- 68. a) J.-Y. Jung, S. E. Naleway, Y. N. Maker, K. Y. Kang, J. Lee, J. Ha, S. S. Hur, S. Chien, J. McKittrick, ACS Biomater. Sci. Eng. 2019, 5, 2122. b) S. Birchfield, Image Processing and Analysis, Cengage Learning, 2016.
- B. Emon, J. Bauer, Y. Jain, B. Jung, T. Saif, Comput. Struct. Biotechnol. J. 2018, 16, 279.
- a) S. S. Hur, Y. Zhao, Y.-S. Li, E. Botvinick, S. Chien, *Cell. Mol. Bioeng.* 2009, 2, 425. b) S. S. Hur, J. C. del Álamo, J. S. Park, Y.-S. Li, H. A. Nguyen, D. Teng, K.-C. Wang, L. Flores, B. Alonso-Latorre, J. C. Lasheras, S. Chien, *Proc. Natl. Acad. Sci.* 2012, 109, 11110.
- a) J. R. Tse, A. J. Engler, Curr. Protoc. Cell Biol. 2010, 47, 10.16,
 b) L. B. Hazeltine, C. S. Simmons, M. R. Salick, X. Lian, M. G. Badur, W. Han, S. M. Delgado, T. Wakatsuki, W. C. Crone, B. L. Pruitt, S. P. Palecek, Int. J. Cell Biol. 2012, 1, 508294.

- 72. a) J.-Y. Tinevez, N. Perry, J. Schindelin, G. M. Hoopes, G. D. Reynolds, E. Laplantine, S. Y. Bednarek, S. L. Shorte, K. W. Eliceiri, *Methods* 2017, 115, 80. b) D. Ershov, M.-S. Phan, J. W. Pylvänäinen, S. U. Rigaud, L. L. Blanc, A. Charles-Orszag, J. R. W. Conway, R. F. Laine, N. H. Roy, D. Bonazzi, G. Duménil, G. Jacquemet, J.-Y. Tinevez, *Nat. Methods* 2022, 19, 829.
- a) S. Srinivasan, S. Das, V. Surve, A. Srivastava, S. Kumar, N. Jain,
 A. Sawant, C. Nayak, R. Purwar, Sci. Rep. 2019, 9, 19930. b) Y.-T.
 Yeh, R. Serrano, J. François, J.-J. Chiu, Y.-S. J. Li, J. C. Del Álamo,
 S. Chien, J. C. Lasheras, Proc. Natl. Acad. Sci. 2018, 115, 133.
- N.-A. Pham, N. Radulovich, E. Ibrahimov, S. N. Martins-Filho, Q. Li, M. Pintilie, J. Weiss, V. Raghavan, M. Cabanero, R. E. Denroche, J. M. Wilson, C. Metran-Nascente, A. Borgida, S. Hutchinson, A. Dodd, M. Begora, D. Chadwick, S. Serra, J. J. Knox, S. Gallinger, D. W. Hedley, L. Muthuswamy, M.-S. Tsao, Sci. Rep. 2021, 11, 10619.
- A. Dheeraj, F. J. Garcia Marques, D. Tailor, A. Bermudez, A. Resendez, M. Pandrala, B. Grau, P. Kumar, C. B. Haley, A. Honkala, P. Kujur, S. S. Jeffrey, S. Pitteri, S. V. Malhotra, *Cell Rep. Med.* 2024, 5, 101552.

W. Qiu, Y. Zheng, F. Shen, Z. Wang, Q. Huang, W. Guo, Q. Wang,
 P. Yang, F. He, Z. Cao, J. Cao, ACS Appl. Mater. Interfaces 2024,
 16, 61679.

SUPPORTING INFORMATION

Additional supporting information can be found online in the Supporting Information section at the end of this article.

How to cite this article: L. D. Anggradita, J. H. Kim, M.-K. Kim, J. W. Son, M. Farhan, J. S. A. Jeberson, A. Taghizadeh, H.-W. Kim, J. H. Park, J. Yang, H. K. Byeon, S. S. Hur, M. J. Ban, Y. Hwang, *VIEW.* **2025**, 20240089.

https://doi.org/10.1002/VIW.20240089